A DETECTOR TO MEASURE ^{9}Li PRODUCTION RATE IN LIQUID SCINTILLATOR AT THE EARTH'S SURFACE BY COSMIC RAY MUONS

by

MARK A. SMITH

B.S., Washburn University, 2001

AN ABSTRACT OF A DISSERTATION

submitted in partial fulfillment of the
requirements for the degree

DOCTOR OF PHILOSOPHY

Department of Physics
College of Arts and Sciences

KANSAS STATE UNIVERSITY
Manhattan, Kansas
2009

Abstract

The next generation of nuclear fission reactor based neutrino experiments seeking to measure the θ_{13} mixing angle rely upon measurements made by detectors placed close to the reactor, and therefore less shielded from cosmic ray muons by the earth. ^{9}Li production in liquid scintillator by these cosmic ray muons becomes a serious problem for these experiments that must be dealt with since the ^{9}Li production rate is still a significant fraction of the neutrino interaction rate. This ^{9}Li background reduces the experiment's sensitivity to measure the θ_{13} mixing angle. This thesis discusses a small detector designed to measure the ^{9}Li production rate in liquid scintillator at the earth's surface by cosmic ray muons. The detector was designed, built, and finally, calibrated. The ability to find the signals necessary to actually measure the ^{9}Li production rate is shown, establishing that this detector will be able to measure the production rate. A 90% significance level upper limit for the ^{9}Li-like production rate, based on only 3.5 days worth of data, is reported as 213 ^{9}Li-like events per day per ton.

A DETECTOR TO MEASURE ^{9}Li PRODUCTION RATE IN LIQUID SCINTILLATOR AT THE EARTH'S SURFACE BY COSMIC RAY MUONS

by

Mark A. Smith

B.S., Washburn University, 2001

A DISSERTATION

submitted in partial fulfillment of the
requirements for the degree

DOCTOR OF PHILOSOPHY

Department of Physics
College of Arts and Sciences

KANSAS STATE UNIVERSITY
Manhattan, Kansas
2009

Approved by:

Major Professor
Glenn Horton-Smith

Copyright

Abstract

The next generation of nuclear fission reactor based neutrino experiments seeking to measure the θ_{13} mixing angle rely upon measurements made by detectors placed close to the reactor, and therefore less shielded from cosmic ray muons by the earth. ^{9}Li production in liquid scintillator by these cosmic ray muons becomes a serious problem for these experiments that must be dealt with since the ^{9}Li production rate is still a significant fraction of the neutrino interaction rate. This ^{9}Li background reduces the experiment's sensitivity to measure the θ_{13} mixing angle. This thesis discusses a small detector designed to measure the ^{9}Li production rate in liquid scintillator at the earth's surface by cosmic ray muons. The detector was designed, built, and finally, calibrated. The ability to find the signals necessary to actually measure the ^{9}Li production rate is shown, establishing that this detector will be able to measure the production rate. A 90% significance level upper limit for the ^{9}Li-like production rate, based on only 3.5 days worth of data, is reported as 213 ^{9}Li-like events per day per ton.

Table of Contents

List of Figures

List of Tables

Acknowledgments

From seven years of work at Kansas State, there are many people to thank. First, let me thank my advisor Glenn Horton-Smith for all of his help and advice. Tim Bolton has been a great source of advice as well. Thanks for the recommendation to the Lindau meeting with Nobel laureates. It was a trip to remember forever. Pamela, our HEP secretary, has always been a diligent worker to make sure that I got paid, or a rental car, or a plane ticket. Thanks for making those administrative things easier.

Outside of HEP, I am grateful for the expertise of the guys in the Machine Shop, Russ Taylor and Bryan Merrill. The boxes you built for us exceeded expectations. Al Rankin and Mike Wells were always available to lend needed tools or to give mechanical advice. Thank you. I also want to thank Kevin Carnes for letting me borrow the Octal CFD. Without it this research would not have been possible.

I would also like to thank the members of my committee, Glenn Horton-Smith, Tim Bolton, Noel Stanton, Larry Weaver, Dave Auckly, and Anil Pahwa for taking time to consider my dissertation.

Dedication

To Christy

"Through faith we understand that the worlds were framed by the word of God, so that things which are seen were not made of things which do appear."

–Hebrews 11:3

Chapter 1

The History of the Neutrino

The history of experimental particle physics is full of particle discoveries, each with its own unique story. None, perhaps, is as unique as the story of the discovery of the neutrino, for the neutrino was invented before it was discovered. In 1930, physicists were grappling with two problems. The idea of a quantum mechanical spin for each particle had already been developed. They were also discovering the behavior that distinguished between particles that were fermions and those that were bosons. The problem was that ^{14}N and ^{6}Li appeared to have "wrong" statistics. In addition, since beta decay was proposed to be a two-body decay, energy conservation required the accompanying β electron to have a specific energy. This electron was instead observed to have a spectrum of energy values. Pauli was inspired to solve this problem by inventing a spin 1/2 particle, and thus a fermion, with no electric charge that he called a "neutron" [1]. Pauli imagined that this new particle was emitted along with the electron in beta decay, thus solving the discrepancy in energy conservation. He also imagined that this "neutron" inhabited the nucleus, helping to resolve the spin problem.

Two years later, J. Chadwick experimentally observed a neutral particle that inhabited the nucleus, calling it a neutron, but this particle was not quite the one that Pauli had imagined[2,3]. In 1934, Enrico Fermi explained the continuous beta energy spectrum by describing beta decay as Chadwick's neutron decaying into a proton, the β electron, and Pauli's invisible particle now called a neutrino (Italian for "little neutral one")[4,5]:

$$n \rightarrow p + e^{-} + \bar{\nu}.$$

The neutrino could thus have mass equal to or less than the electron and no electric charge. Fermi saw this interaction as analogous to photon emission from an atom, opening the door to understanding the weak nuclear force.

The neutrino then had a theoretical basis, but it would be nearly two decades before it was directly observed. In 1946 Pontecorvo had put forward the idea that neutrinos could be observed via inverse beta decay, $p + \bar{\nu} \rightarrow n + e^{+}$ [6]. Reines and Cowan then developed a delayed-coincidence experiment to observe this interaction[7]. Needing a source of anti-electron neutrinos, they initially considered using a nuclear blast, but later settled on reactor anti-neutrinos. The basic idea was to look for light generated in scintillator from the positron as a prompt signal, and then looking for neutron capture on cadmium, which had been dissolved in the liquid scintillator, a few μs later. This basic technique is still common in reactor neutrino experiments. For this discovery, Reines received the Nobel prize in 1995.

After experimental observation of the neutrino, research proceeded in earnest. Davis and Harmer showed that there was a distinction between neutrinos and anti-neutrinos. In 1956 Lee and Yang proposed that the weak interaction, the force involved in neutrino production, was not parity invariant, as had been assumed[8]. C.S. Wu followed up with their proposed experiment later that year[9]. She had carefully aligned ^{60}Co atoms so that their spins pointed in a specific direction, and then observed the direction of electrons that came from their decay. She found that there was a preferred direction for the electrons. In fact, this violation of parity is maximal. It was later confirmed that all neutrinos have left-handed parity (spin and momentum anti-parallel), and all anti-neutrinos have right-handed parity (spin and momentum parallel)[10]. To accommodate this discovery the neutrino was supposed to be massless. From there it was further shown that neutrinos that came from pion decay into muons, now known as muon neutrinos, were distinct from electron neutrinos[11]. The "type" of neutrino is known as its flavor since neutrinos associated with electrons are distinct from

neutrinos associated with muons. The physics of neutrinos was certainly as rich as the rest of the particle realm.

Two large steps in neutrino physics occurred in the 1960s. In the realm of theory, giant strides were made in developing a framework for weak interactions. Electromagnetic theory was then combined with weak force theory, enabling the development of electroweak theory. Key in this endeavor was the work of Glashow in 1961[12], Salam and Ward in 1964[13], and Steven Weinberg in 1967[14]. In addition to the charged-current interaction of the W boson, a neutral current, involving the Z boson, was predicted for the weak interaction.

In the laboratory a key measurement of solar neutrinos was made by Ray Davis. Davis, a physical chemist, built a giant tank of dry-cleaning fluid in the Homestake gold mine 4850 feet below ground to shield his detector from background. It had been determined that a terminal reaction in the proton-proton chain in the fusion reactions of the sun produced neutrinos with enough energy to interact with ^{37}Cl in the dry-cleaning fluid and convert it to ^{37}Ar, which could be readily separated from the fluid. After several years of perfecting the separation and counting technique, the result was shocking. Davis found only one-third of the theoretically expected neutrino flux from the sun[15]. Many were skeptical of Davis' result, doubting the process that separated and counted the Ar from the fluid. Recent results, however, have confirmed Davis' result for electron neutrinos. It turns out that 2/3 of the electron neutrinos produced in the Sun oscillate to the two other flavors of neutrinos as they travel from the Sun's core to its surface. (There are at present three known flavors of neutrinos: electron, muon, and tau.) Davis' technique could only measure electron neutrinos, and thus showed a discrepancy. A more recent experiment sensitive to all three neutrino types finds the expected solar neutrino flux[16].

The discoveries did not end there. The theoretically-predicted weak neutral current $\bar{\nu}_\mu + e^- \rightarrow \bar{\nu}_\mu + e^-$ was observed at CERN in 1976[17,18,19]. A third type of lepton, the τ, was observed in 1978[20,21,22]. The corresponding τ neutrino was seen in 2000[23]. Precise measurements of the Z^0 boson decay width confirmed that there are three light neutrinos[24].

Also, neutrinos from supernova SN1987a were observed by two different water Cherenkov detectors, giving a teasing glimpse into extra-terrestrial neutrinos from a source other than the Sun[25,26].

Recent years have continued to see a flurry of activity in neutrino physics. KamLAND, a reactor anti-neutrino experiment based in Japan that utilizes that nation's many reactors as neutrino sources, observed a clear deficit in anti-electron neutrinos at the average distance L_0 from the reactor sources[27].

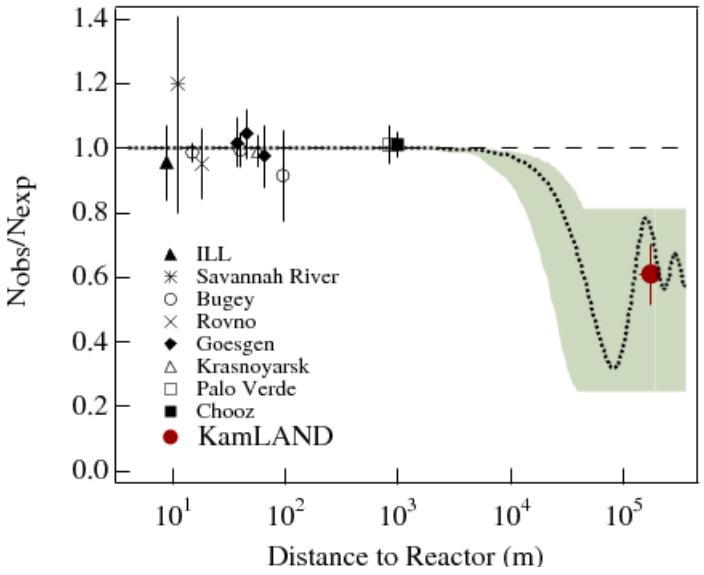

Figure 1.1: *The ratio of measured to expected $\bar{\nu}_e$ flux from various reactor experiments. The solid circle is the KamLAND initial result plotted at a flux-weighted average distance of $\sim 180km$. The dotted curve, $\sin^2 2\theta = 0.833$ and $\Delta m^2 = 5.5 \times 10^{-5} eV^2$, is representative of a best-fit LMA prediction and the dashed curve is expected for no oscillations. LMA is the Large Mixing Angle solution (see chapter 2 for a description).*

More recent results from KamLAND show the spectrum of the ratio of L_0 to anti-neutrino energy. Figure 1.2 below shows the same deficit in anti-neutrino survival probability, but it also reveals a more thorough confirmation of oscillation as the survival probability returns for smaller neutrino energies[28].

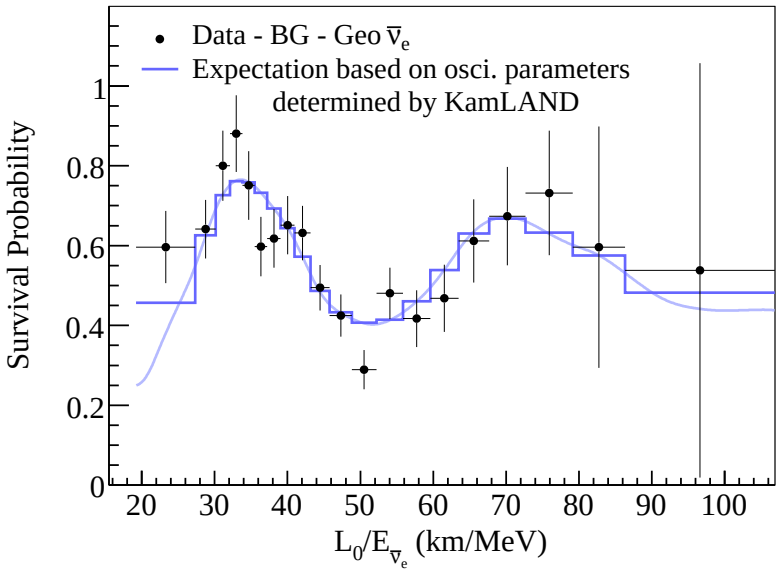

Figure 1.2: *From the KamLAND experiment, the ratio of the $\bar{\nu_e}$ spectrum (with background and geo-neutrino-subtracted) to the expectation for no-oscillation as a function of L_0/E. L_0 is the effective baseline taken as a flux-weighted average($L_0 = 180km$).*

Chapter 2

Neutrino Physics

2.1 Neutrinos in the Standard Model

In the highly successful Standard Model (SM) of particle physics, there are two classes of particles: fermions and bosons. Fermions are themselves made up of two groups, leptons (of which the neutrino is a member) and quarks. Both quarks and leptons have three generations or flavors. Bosons are the force mediators for the three forces included in the SM: the electromagnetic, the weak nuclear, and the strong nuclear forces (gravity, the other known fundamental force, is not included in the SM). Also, note that each particle in the SM has an antiparticle.

For the neutrino, there are three known flavors corresponding to the three charged leptons, the electron (e), the muon (μ), and tau (τ). The neutrinos are then, respectively, ν_e, ν_μ, and ν_τ. Since the neutrino is chargeless and colorless (Color is the name for the strong force charge. Being colorless means the neutrino does not interact via the strong force.), it interacts only via the weak force. There are two types of weak interactions for the neutrino: charged-current interactions involving a W boson exchange, and neutral current interactions with a Z^0 exchange. Figure 2.1 sketches the basic charged current and neutral current interactions.

The SM assumes that the neutrino is massless. Direct searches for the mass of each neutrino flavor have shown that $m_{\nu_e} < 2$ eV , $m_{\nu_\mu} < 0.19$ MeV , and $m_{\nu_\tau} < 18.2$ MeV[29].

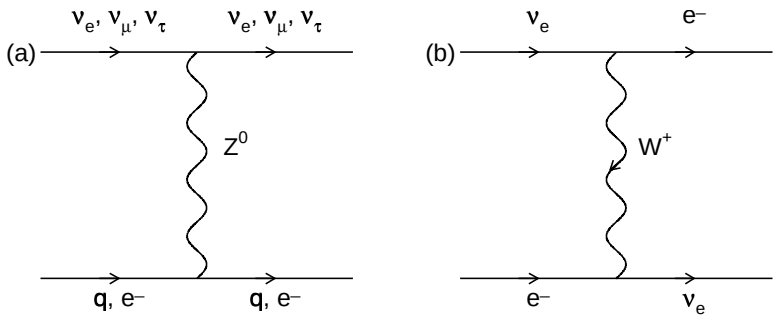

Figure 2.1: *Feynman diagrams for neutrino forward scattering in matter. All neutrinos experience the neutral coupling shown in (a), but only electron neutrinos experience the charged coupling of (b).*

The tightest present constraint on neutrino mass comes from combining cosmological and neutrino oscillation data, $\sum m_\nu < 0.17$ eV[29]. The massless character of SM neutrinos means that all neutrinos are of left-handed helicity (Helicity is the relationship between spin direction and momentum direction. Left-handed is anti-parallel. Right-handed is parallel.) and all anti-neutrinos are of right-handed helicity.

2.2 Neutrino Oscillations

While the Standard Model assumes the neutrino to be massless, theorists have conjectured for decades that this might not be so. Pontecorvo first proposed mixing between neutrinos and anti-neutrinos as early as 1957[30,31,32], though it was in 1962 that Z. Maki, M. Nakagawa, and S. Sakata proposed the mixing between generations of neutrinos that we know today[33].

Quantum mechanical oscillations in particles occur between two or more states when those states have different masses and are not eigenstates of some force. Neutrinos created in interactions are generally not mass eigenstates, but are instead flavor eigenstates represented by $|\nu_e\rangle$, $|\nu_\mu\rangle$, and $|\nu_\tau\rangle$. These flavor eigenstates need not correspond with the mass eigenstates denoted as $|\nu_1\rangle$, $|\nu_2\rangle$, and $|\nu_3\rangle$. In the standard representation for neutrinos, the flavor and mass eigenstates each form a complete basis that describes the set of neutrinos.

Each basis then can be expressed as a linear combination of the other basis. For example, to write each flavor eigenstate in terms of the mass eigenstates,

$$|\nu_\alpha\rangle = \sum_i U^*_{\alpha\iota}|\nu_\iota\rangle, \tag{2.1}$$

where $U^*_{\alpha\iota}$ represents the mixing between the two bases, $|\nu_\alpha\rangle$ is the flavor eigenstate, and $|\nu_\iota\rangle$ is a mass eigenstate. Further, $|U^*_{\alpha\iota}|^2$ reveals the fraction of mass state i in flavor state α.

The elements $U^*_{\alpha\iota}$ are combined into a mixing matrix U. For three generations this is written as:

$$U = \begin{pmatrix} U_{e1} & U_{e2} & U_{e3} \\ U_{\mu 1} & U_{\mu 2} & U_{\mu 3} \\ U_{\tau 1} & U_{\tau 2} & U_{\tau 3} \end{pmatrix}. \tag{2.2}$$

This three-generation mixing matrix can be decomposed into three matrices, each representing two-state mixing:

$$U = \begin{pmatrix} 1 & 0 & 0 \\ 0 & c_{23} & s_{23} \\ 0 & -s_{23} & c_{23} \end{pmatrix} \begin{pmatrix} c_{13} & 0 & s_{13}e^{-\iota\delta} \\ 0 & 1 & 0 \\ -s_{13}e^{-\iota\delta} & 0 & c_{13} \end{pmatrix} \begin{pmatrix} c_{12} & s_{12} & 0 \\ -s_{12} & c_{12} & 0 \\ 0 & 0 & 1 \end{pmatrix} \tag{2.3}$$

where $c_{ij} = \cos\theta_{ij}$, $s_{ij} = \sin\theta_{ij}$, and δ is the CP violating phase. The first matrix represents ν_μ to ν_τ mixing, the second ν_e to ν_τ mixing, and the third ν_e to ν_μ mixing. It should be noted that this matrix applies for Dirac-type neutrinos (that neutrinos are truly distinct particles from anti-neutrinos). If neutrinos are Majorana-type (that neutrinos and anti-neutrinos are actually the same particle with no distinction between them) then there are two additional complex phases α_1 and α_2.

2.2.1 Oscillations in Vacuum

Consider a flavor eigenstate $|\nu_\alpha\rangle$ created in vacuum with momentum p in a two mass state regime. As the neutrino travels, the two mass states have slightly different velocities, causing the flavor content of the neutrino to vary with time. Expressed in the standard way, the

time dependence of state ν_α which was solely $|\nu_\alpha\rangle$ at $t = 0$ is:

$$|\nu_\alpha\rangle_t = \exp(\frac{-iE_1t}{\hbar})|\nu_1\rangle\cos\theta + \exp(\frac{-iE_2t}{\hbar})|\nu_2\rangle\sin\theta. \tag{2.4}$$

The probability that the particle will be observed as flavor $|\nu_\beta\rangle$ at time t is

$$P_{\alpha\to\beta} = |\langle\nu_\beta|\nu_\alpha\rangle_t|^2 = \sin^2 2\theta \sin^2(\frac{1}{2}(E_2 - E_1)t). \tag{2.5}$$

For neutrinos, we can assume that $E_i \gg m_i$, so in the ultra-relativistic approximation, and with $\hbar = c = 1$:

$$E_i = \sqrt{p^2 + m_i^2} \approx p + \frac{m_i^2}{2p} = E + \frac{m_i^2}{2E}. \tag{2.6}$$

Then,

$$E_2 - E_1 \approx \frac{m_2^2 - m_1^2}{2E}. \tag{2.7}$$

Since taking c = 1 gives $L = t$, the probability of flavor change becomes:

$$P_{\alpha\to\beta} = \sin^2 2\theta \sin^2(1.27\frac{\Delta m^2 L}{E}). \tag{2.8}$$

where L is the distance traveled by the neutrino in km, E is the neutrino energy in GeV, $\Delta m^2 = m_i^2 - m_j^2$ is in units of eV^2, and 1.27 comes from converting everything over to GeV units that cancel out.

This equation is the fundamental result for neutrino oscillations. Of course, this has been a simple treatment of a much more complicated situation, but it turns out that more rigorous treatments yield the same basic result. The essence of oscillation is captured in this simple equation. Note that for many experiments the probability that the neutrino *doesn't* decay into another flavor is at issue. In the two-neutrino case, the probability that it does not change flavor is unity minus the probability that it does:

$$P_{\alpha\to\alpha} = 1 - \sin^2 2\theta \sin^2(1.27\frac{\Delta m^2 L}{E}). \tag{2.9}$$

2.2.2 Oscillations in Matter

While neutrino oscillation can be readily sketched in vacuum, what happens when oscillation is considered in matter? This question is more than academic for the effect can be dramatic. In reactor neutrino experiments such as KamLAND, the anti-neutrinos from the reactors traverse the earth before reaching the detector. The same applies for long baseline accelerator experiments. However, the most notable matter effects are in the Sun, where the extreme densities have interesting consequences. Matter effects were first described by Wolfenstein, and then further explored by Mikheev and Smirnov.

While traveling through matter, neutrinos can interact with matter by W exchange (charged-current interactions (CC)), and by Z^0 exchange (neutral current interactions (NC)). See Figure 2.1 above. The result is a potential energy that depends upon neutrino flavor. Electron neutrinos, the only neutrino to interact via the CC channel since ordinary matter is composed of electrons but not muons or taus, pick up a potential

$$V_W = +\sqrt{2}G_F N_e \tag{2.10}$$

where N_e is electron number density and G_F is Fermi's constant. Quarks and electrons interact with neutrinos to produce the neutral current potential, but the interaction for protons and electrons are equal but opposite in sign. As a result, only neutrons contribute for the neutral current, depending upon neutron density N_n:

$$V_Z = -\frac{\sqrt{2}}{2}G_F N_n. \tag{2.11}$$

Assuming a two-state system, the Hamiltonian of the system is,

$$H_M = H_{vac} + V_W \begin{pmatrix} 1 & 0 \\ 0 & 0 \end{pmatrix} + V_Z \begin{pmatrix} 1 & 0 \\ 0 & 1 \end{pmatrix}. \tag{2.12}$$

We are looking for differences caused by oscillation in matter, so the V_Z term, which affects all flavors equally and is a multiple of the identity matrix, can be ignored. Cleverly rewriting

V_W, we find the matter Hamiltonian:

$$H_M = H_{vac} + \frac{V_W}{2}\begin{pmatrix} 1 & 0 \\ 0 & -1 \end{pmatrix} + \frac{V_W}{2}\begin{pmatrix} 1 & 0 \\ 0 & 1 \end{pmatrix} \tag{2.13}$$

$$= H_{vac} + \frac{V_W}{2}\begin{pmatrix} 1 & 0 \\ 0 & -1 \end{pmatrix}. \tag{2.14}$$

H_{vac} can be written as

$$H_{vac} = \frac{\Delta m^2}{4E}\begin{pmatrix} -\cos 2\theta & \sin 2\theta \\ \sin 2\theta & \cos 2\theta \end{pmatrix}. \tag{2.15}$$

Then H_M becomes, by introducing a parameter x,

$$H_M = \frac{\Delta m^2}{4E}\begin{pmatrix} -(\cos 2\theta - x) & \sin 2\theta \\ \sin 2\theta & (\cos 2\theta - x) \end{pmatrix}, \tag{2.16}$$

in which

$$x \equiv \frac{V_W/2}{\Delta m^2/4E} = \frac{2\sqrt{2}G_F N_e E}{\Delta m^2}. \tag{2.17}$$

The parameter x is then a measure of the relative importance of the matter effect to the neutrino squared-mass splitting.

To see the physical effect of this matter Hamiltonian, let us make two substitutions. Define

$$\Delta m^2_M \equiv \Delta m^2 \sqrt{\sin^2 2\theta + (\cos 2\theta - x)^2} \tag{2.18}$$

and

$$\sin^2 2\theta_M \equiv \frac{\sin^2 2\theta}{\sin^2 2\theta + (\cos 2\theta - x)^2}. \tag{2.19}$$

The Hamiltonian in matter is finally then,

$$H_M = \frac{\Delta m^2_M}{4E}\begin{pmatrix} -\cos 2\theta_M & \sin 2\theta_M \\ \sin 2\theta_M & \cos 2\theta_M \end{pmatrix}. \tag{2.20}$$

Notice that the matter result is identical in form to the vacuum Hamiltonian, H_{vac}, with the squared-mass splitting and mixing angle terms being replaced with a matter equivalent. If the electron density is approximately constant from between the source and the detector, then the matter oscillation probability is

$$P_M(\nu_\alpha \to \nu_\beta) = \sin^2 2\theta_M \sin^2 \Delta m^2_M \frac{L}{4E}. \tag{2.21}$$

Exactly how large the matter effect is depends upon the type experiment being conducted. For KamLAND, $x \ll 1$. For an accelerator-generated neutrino experiment with a distance from source to target of $\sim$ 1000 km, the beam travels through the earth's mantle, encountering a larger electron density. In that case,

$$|x| \approx \frac{E}{12 \text{ GeV}}. \tag{2.22}$$

If the neutrino energy is a few GeV, then the matter effect is modest. However, if the beam has neutrino energy of 20 GeV, then the effect is significant[34].

For the sun, where electron densities are extremely high, the result of matter interaction is that all neutrinos leaving the sun are in mass eigenstate $|\nu_2\rangle$. The consequence of this is that when an experiment on earth looks for electron neutrinos from the Sun, fewer than expected are found. Recall that

$$|\nu_e\rangle = |\nu_1\rangle \cos\theta + |\nu_2\rangle \sin\theta \tag{2.23}$$

in general. But if the Sun only produces ν_e neutrinos that then oscillate by matter interactions into the mass state ν_2, then for an experiment looking to measure the solar electron neutrino flux,

$$P_{\nu_{e_{sol}} \to \nu_e} = |\langle \nu_e | \nu_{e_{sol}} \rangle|^2 = \sin^2\theta. \tag{2.24}$$

When this experiment is performed, one finds only about 1/3 of the expected electron neutrino flux[35]. This highly suggests that the mass state $|\nu_2\rangle$ is composed of more than $|\nu_e\rangle$, and that some of the electron neutrinos in the sun have oscillated into the other neutrino flavors.

2.2.3 Mixing Parameters

Since neutrinos have been shown to oscillate, the next step in the process of discovery is to measure the neutrino mass and mixing parameters. This goal is a tremendous undertaking and requires the use of accelerator, atmospheric, reactor, and solar neutrino sources. As seen in section 2.2.1 above, neutrino oscillations depend upon the difference of the squares of the

masses involved, of which there are two (Δm^2_{21} and Δm^2_{32}, where $\Delta m^2_{ij} = m(\nu_i)^2 - m(\nu_j)^2$), three mixing angles ($\theta_{12}$, θ_{23}, and θ_{13}), and a CP-violating phase (δ). Assuming there exist only three neutrino flavors, the present experimental situation can be summarized by two essentially decoupled oscillations characterized by "atmospheric" and "solar/reactor" mass squared splittings $\Delta m^2_{atm} = \Delta m^2_{32}$ and $\Delta m^2_{sol} = \Delta m^2_{21}$ with the corresponding mixing angles $\theta_{atm} = \theta_{23}$ and $\theta_{sol} = \theta_{12}$. It turns out that θ_{12} and θ_{23} are surprisingly large, the so-called Large Mixing Angle solution (LMA). Present best values reveal $\sin^2 2\theta_{12} = 0.86^{+0.03}_{-0.04}$ and $\sin^2 2\theta_{23} > 0.92$. Also, $\Delta m^2_{21} = (8.0 \pm 0.3) \times 10^{-5}\text{eV}^2$ and $\Delta m^2_{23} = (1.9 - 3.0) \times 10^{-3}\text{eV}^2$. The third mixing angle, θ_{13} has been shown by the CHOOZ experiment to be small, $\sin^2 2\theta_{13} < 0.19$[29]. The smallness of θ_{13} contributes to the essentially decoupled nature of atmospheric and solar/reactor neutrino oscillations. Consider for example the three-neutrino solution for reactor anti-neutrinos (compare with the two-neutrino solution in equation (2.9)):

$$P(\bar{\nu_e} \to \bar{\nu_e}) \cong 1 - \sin^2 2\theta_{13} \sin^2 \frac{\Delta m^2_{atm} L}{4E} - \cos^4 \theta_{13} \sin^2 2\theta_{12} \sin^2 \frac{\Delta m_{12} L}{4E}. \tag{2.25}$$

Two mixing angles are now involved. The two neutrino solution assumed that reactor anti-neutrino mixing depended solely upon θ_{12}. For the three neutrino model there is a θ_{13} dependence as well. The behavior of this probability function is plotted for the given parameters in Figure 2.2 below. Notice that for a small θ_{13} angle, equation (2.25) becomes equation (2.9).

To proceed beyond our current understanding of neutrino physics more precise measurements of these parameters need to be obtained, including confirming whether θ_{13} is large enough to observe CP-violation governed by the parameter δ. In fact, it first needs to be determined that θ_{13} is finite to confirm genuine three-flavor oscillation. This is the goal of the next generation of reactor neutrino experiments such as Daya Bay and Double Chooz. The basic idea of these experiments is to use two identical detectors, one close to the reactor to determine the nominal flux of neutrinos from the reactor, and then a further detector placed at the first θ_{13} minimum to measure a deviation from this nominal flux. Any deviation would determine the size of θ_{13}. (See Figure 2.3 below.) If $\theta_{13} \geq 0.01$ then

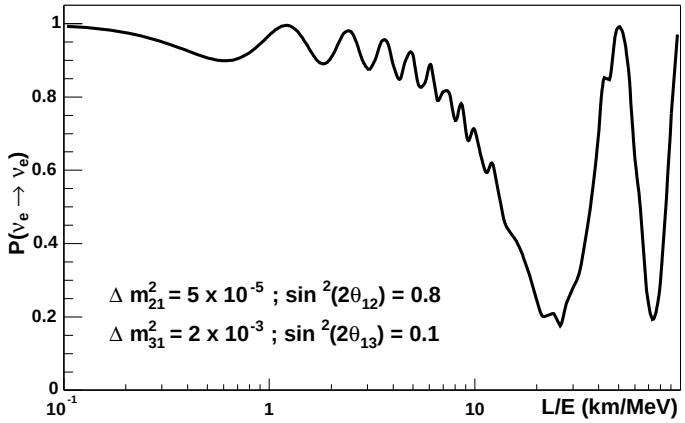

Figure 2.2: *Probability of ν_e disappearance versus L/E for θ_{13} at its current upper limit.*

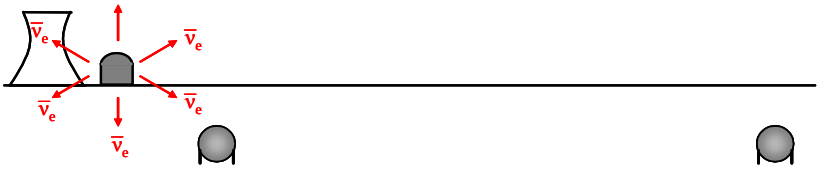

Figure 2.3: *Schematic layout of a two-detector reactor neutrino oscillation experiment.*

straightforward extensions of current experiments can be carried out to determine not only the value of the CP-violating phase δ, but to determine the sign of the mass splitting Δm_{32}. As Figure 2.4 indicates, determining the sign of Δm_{32} will reveal the neutrino mass hierarchy, i.e. is the mass of ν_3 greater than ν_2 and ν_1 or less than them both? Note that the LMA theory assumes $\nu_2 > \nu_1$.

2.3 CP and CPT

No discussion of neutrino physics can be complete without mentioning the hallmark of the weak interaction, parity invariance violation, and the related CP violation and CPT theorem. C, P, and T refer to three potential symmetries in nature: Charge conjugation, parity, and time reversal symmetry.

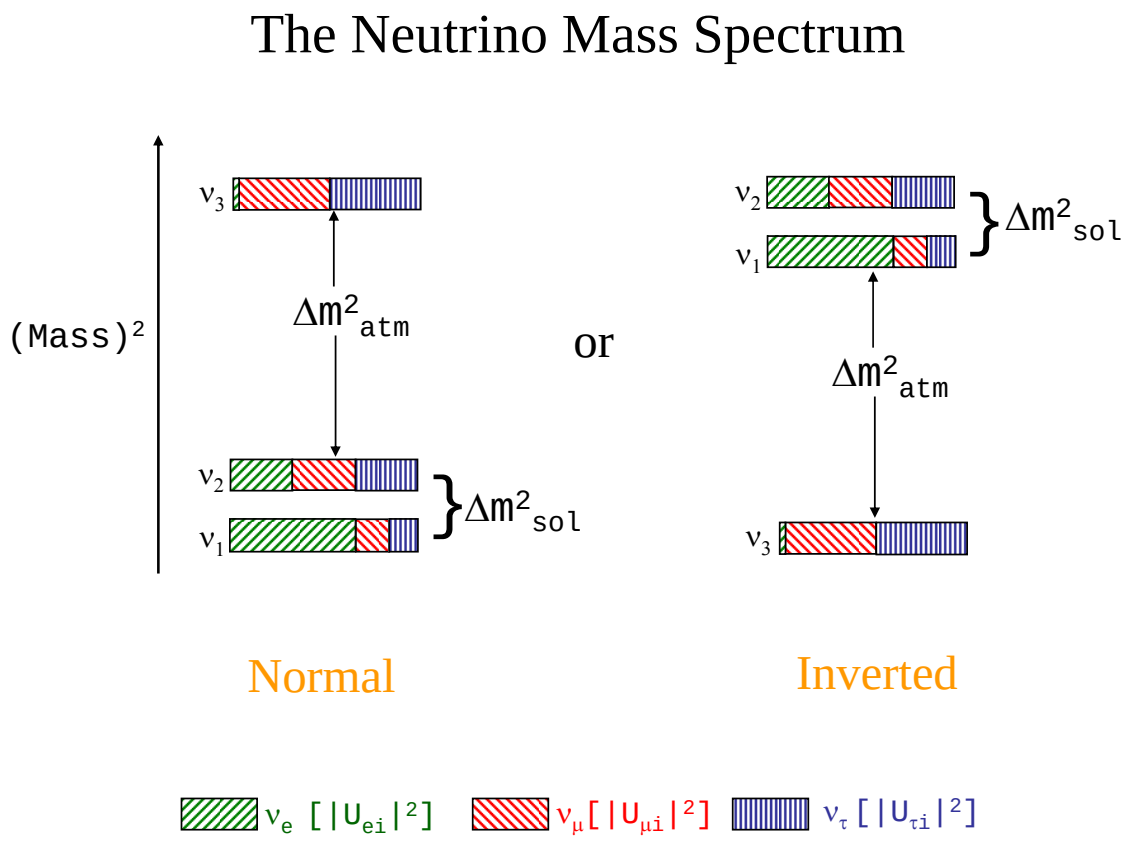

Figure 2.4: *The two possible neutrino (mass)^2 spectrums assuming only three neutrinos. Included is the flavor fraction composition for each mass eigenstate.*

Let us begin with discussing parity[36]. Before 1956 it was taken for granted that the laws of physics operated the same for a physical process and its mirror-image. This mirror symmetry is known as parity invariance. By way of definition, parity is the operation where a point is inverted through the origin to a position diametrically opposite to it. In a three-dimensional situation this is the same as the transformation (x,y,z) $\rightarrow$ (-x,-y,-z).

In 1956 Lee and Yang searched the literature to find evidence for any experimental tests of parity invariance[8]. They found plenty of evidence in electromagnetic and strong processes, but no evidence for weak interactions. They then proposed a test of parity invariance for weak interactions, later carried out by C. S. Wu[9]. Radioactive ^{60}Co was carefully aligned so

that their spins were all in the z direction (pointing north). When a ^{60}Co atom underwent β decay, the direction of the emitted electron was recorded. It was discovered that all of the electrons came out in the northerly direction, that is in the direction of the nuclear spin. This result was a clear violation of parity invariance, as the mirror image would be a ^{60}Co atom oriented in the -z direction (pointing south). The electrons would then still have to come off in the northerly direction, but that would be opposite to the spin, which is pointing south in the mirror image. This result is not allowed, so parity invariance is violated.

Once it was observed, physicists realized that parity violation is maximal for the weak force. The most dramatic proof of this is with neutrinos. Imagine setting the z-axis along the direction a neutrino is traveling. Then the z component of spin is either parallel or anti-parallel with this direction. It turns out that all neutrinos have anti-parallel spins (left-handed) and all anti-neutrinos have parallel spins (right-handed). This is maximum violation of parity invariance.

2.3.1 CP Violation

Let us look at charge conjugation symmetry. Charge conjugation converts a particle to its anti-particle, changing the sign of all internal quantum numbers. Internal quantum numbers include electric charge, baryon number, lepton number, strangeness, and the like. Quantities such as mass, energy, momentum, and spin are unchanged. While the strong and electromagnetic interactions preserve C invariance, the weak force does not. Recall all neutrinos are left-handed. When applied to a neutrino C gives a left-handed anti-neutrino. No such particle has been observed in nature. Once again, the weak force violates another symmetry.

Combining C and P together might provide a solution for our concern over these symmetry violations, however. The weak force violates C and P, so if they are taken together, CP should be preserved. Perhaps CP is what we originally meant when we thought of a mirror-image, not just inversion through the origin, but conversion of particles to anti-particles as

well.

This idea was put to the test by Gell-Mann and Pais[37]. They proposed a strange test of CP invariance using neutral K mesons. Due to a second-order weak interaction K^0 is able to transform into $\bar{K^0}$ and vice versa. It is then possible to define two states that are superpositions of K^0 and $\bar{K^0}$ and yet eigenstates of CP:

$$|K_1\rangle = \frac{1}{\sqrt{2}}(|K^0\rangle - |\bar{K^0}\rangle) \text{ and } |\mathrm{K}_2\rangle = \frac{1}{\sqrt{2}}(|\mathrm{K}^0\rangle + |\bar{\mathrm{K}^0}\rangle) \tag{2.26}$$

with

$$CP|K_1\rangle = |K_1\rangle \text{ and } CP|\mathrm{K}_2\rangle = -|\mathrm{K}_2\rangle. \tag{2.27}$$

Assuming CP is conserved in weak interactions, K_1 can only decay into a state with CP = +1, and K_2 can only decay into a state with CP = -1. From experiment it was known by Gell-Mann and Pais that neutral kaons usually decayed into states with two or three pions. Pions are eigenstates of C with an eigenvalue of +1. Also, a two pion state has parity +1, and a three pion state has parity -1. Thus, K_1 should decay into two pions (but never three) and K_2 into three (but never two). Now, due to available phase space, the 2π decay happens much faster than 3π. So, starting with an initial beam of K^0's

$$|K^0\rangle = \frac{1}{\sqrt{2}}(|K_1\rangle + |K_2\rangle) \tag{2.28}$$

the K_1 component will decay away quickly. Down the beam line there should be beam of pure K_2's. Stated another way, Gell-Mann and Pais predicted that near the source there should be mostly 2π decays while further on only 3π decays should be expected. When measured, the prediction of Gell-Mann and Pais was confirmed[38].

This was an exciting example of theory predicting experimental results that people considered unorthodox, but more was to come from this experiment. Gell-Mann and Pais made their prediction before parity invariance was discovered to be violated. They assumed CP was a valid symmetry, but was it? If CP is a valid symmetry, this experiment should produce an arbitrarily pure beam of the long-lived K_2 species. If at this point we observe 2π

decays, we know CP has been violated. Cronin and Fitch performed such an experiment in 1964[39]. They built a 57 feet long beam line, and found 45 two-pion decays out of a total of 22,700 decays. That is a small deviation, roughly one in 500, but it is significant because it is an unmistakable violation of CP invariance. Apparently, the long-lived neutral kaon is not a perfect eigenstate of CP, but it instead has a small admixture of K_1:

$$|K_L\rangle = \frac{1}{\sqrt{1+|\epsilon|^2}}(|K_2\rangle + \epsilon|K_1\rangle) \tag{2.29}$$

The coefficient ϵ is a measure of the weak force's departure from CP invariance; experimentally its value is about 2.3×10^{-3}.

2.3.2 CPT

With the fall of CP invariance the last hope for some kind of exact mirror symmetry in nature was destroyed. But, one final test remains. There is one remaining potential symmetry, time-reversal. Time-reversal is the symmetry that physics processes should be independent of the direction of time. Studies of strong force and electromagnetic interactions reveal that they are time-reversal invariant, but weak force interactions are difficult to check for time-reversal symmetry. Despite this there is a compelling reason to think that the weak force is not invariant under time-reversal. Quantum field theory predicts that CPT must be an exact symmetry of any interaction. Given that CP is violated by the weak interaction, then T must be violated so that the combination CPT holds as an exact symmetry.

2.3.3 CP Violation in Neutrinos

Lastly, a brief discussion about the CP-violating parameter δ. From equation (2.3) it is seen that the parameter δ appears as part of a complex exponential term. This is important because a more thorough development of the probability of neutrino oscillation (assuming CPT invariance) shows that the oscillation probability depends upon whether the mixing matrix U is complex or simply real (see Figure 2.5)[34].

$$\mathrm{P}(\overset{(-)}{\nu_\alpha} \to \overset{(-)}{\nu_\beta}) = \delta_{\alpha\beta} - 4\sum_{i>j} \Re(U^*_{\alpha i}U_{\beta i}U_{\alpha j}U^*_{\beta j}) \sin^2(\Delta m^2_{ij}\frac{L}{4E}) \\ \overset{+}{(-)} 2\sum_{i>j} \Im(U^*_{\alpha i}U_{\beta i}U_{\alpha j}U^*_{\beta j}) \sin(\Delta m^2_{ij}\frac{L}{2E})$$

Figure 2.5: *The general expression for the oscillation probability of a neutrino, assuming CPT invariance.*

From this result it is observed that the oscillation probabilities $\mathrm{P}(\bar{\nu_\alpha} \to \bar{\nu_\beta})$ and $\mathrm{P}(\nu_\alpha \to \nu_\beta)$ will differ if U is complex. Since $\bar{\nu_\alpha} \to \bar{\nu_\beta}$ and $\nu_\alpha \to \nu_\beta$ are CP-mirror images, $\mathrm{P}(\bar{\nu_\alpha} \to \bar{\nu_\beta})$ $\neq \mathrm{P}(\nu_\alpha \to \nu_\beta)$ would be an indication of CP-violation. Remember that in equation (2.3) U is complex only if the CP-violating parameter δ is non-zero. Observing CP-violation would confirm that δ is non-zero, and a measurement of its value could then be made. Note that CP-violation has so far only been observed in the quark sector. Observing CP-violation in neutrino oscillation would certainly be interesting, and would open up more opportunities to investigate the physical behavior of neutrinos.

Neutrino oscillation is an exciting subject in contemporary physics. It is critical that we measure the relevant mixing parameters as accurately as possible to better understand neutrino physics. To this end it is generally agreed that the next major step is to determine the scale of θ_{13} so that further experiments may be optimally designed to more precisely determine the other mixing parameters.

Chapter 3

Detecting Reactor Neutrinos

Reactor anti-neutrino experiments almost universally use the inverse beta decay process $p + \bar{\nu_e} \rightarrow n + e^+$ to detect anti-neutrinos (see figure 3.1).

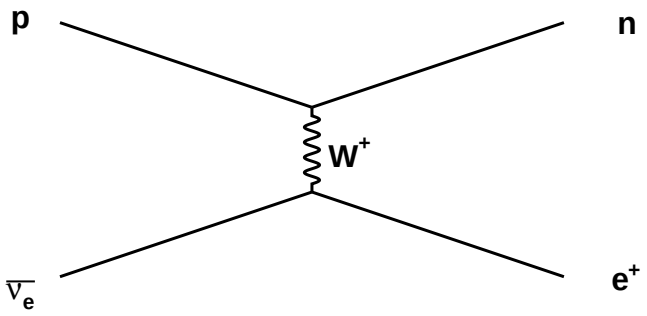

Figure 3.1: *The primary Feynman diagram for the inverse beta interaction in the typical reactor anti-neutrino experiment.*

The e^+ provides a prompt signal as it first slows down and is then annihilated by interaction with an electron. The prompt signal is then followed by the delayed signal of the neutron capture. Requiring the double coincidence of these two signals within a certain time window allows powerful rejection of backgrounds. Typical detector designs allow a relatively high rate of a few Hertz of positron-like signals, but rely on a low rate of neutron-like capture signals to keep the background low. The key factor then for these designs to keep background signals low is to limit the neutron-like signals. This is done in several ways[40]:

1. Eliminate external thermal neutrons since they come uncorrelated with any prompt

signal. Sufficient shielding will eliminate this background.

2. Shield against external fast neutrons. Fast neutrons from outside of the detector can thermalize in the detector, producing a prompt followed by the delayed capture signal.

3. Initiate a muon veto. High-energy muons can produce neutrons in the interior of the detector itself and these neutrons significantly contribute to the neutron background in delayed coincidence experiments. In addition, beta-emitting isotopes might be produced in the same event. A neutron capture then appears in correlation with a prompt signal. Since neutron capture times are relatively short (typically ≈ 30 μs), an efficient muon veto can eliminate this background.

4. Account for the beta-delayed neutron decays of the isotopes ^{9}Li ($t_{1/2} = 178$ ms) and ^{8}He ($t_{1/2} = 119$ ms). These isotopes are produced by spallation as muons pass through the scintillator and interact with ^{12}C. The beta-delayed decay process produces an electron followed by a neutron, mimicking the anti-neutrino signal.

For the previous series of reactor anti-neutrino experiments, KamLAND and CHOOZ for example, these conditions were sufficient. As discussed in chapter 2, the next goal of neutrino physics is to try to measure the scale of the θ_{13} mixing angle. This will require several improvements over past detector designs. First, the unoscillated neutrino flux must be accurately measured. As seen in figure 2.2, θ_{13} produces a relatively small change in the survival probability of the anti-neutrino. To determine if a decrease in electron anti-neutrino flux has occurred at a given distance, the unoscillated anti-neutrino flux must be known. This measurement will be accomplished at both the Daya Bay and Double Chooz experiments by building two (essentially) identical detectors, one as close to the reactor as feasible, and the other at the appropriate distance to enable the first major decrease in anti-neutrino flux from θ_{13} to be observed. Taking the ratio of the two measurements from essentially identical detectors will enable more of the systematic errors to be eliminated, enabling a measurement of θ_{13} to be obtained.

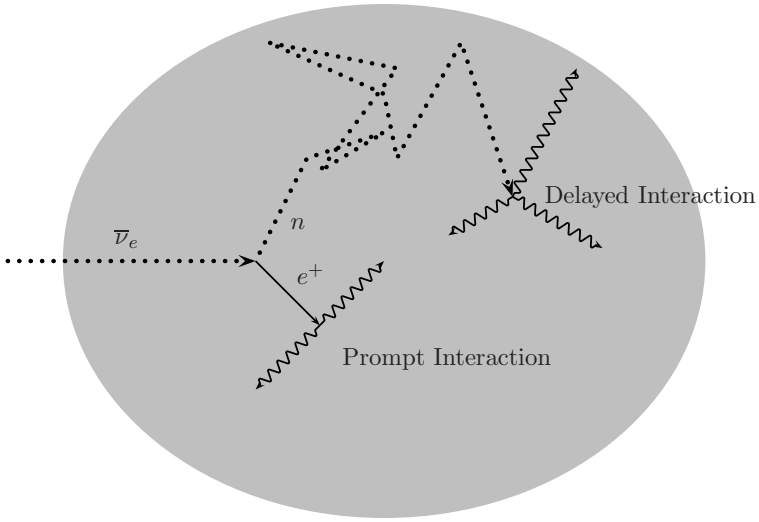

Figure 3.2: *The delayed coincidence signal of inverse beta decay. A neutrino interacts with a proton producing a positron and a neutron. The positron and annihilation gamma rays are visible by their ionization of the detector (prompt interaction). After the neutron thermalizes, it is captured by a nucleus which releases deexcitation gamma rays (delayed interaction)*[41].

Site	Depth [m.w.e.]	Overburden geometry	muon flux $[m^{-2}s^{-1}]$	Events/ton/day neutrons	$^9Li/^8He$
KamLAND	2700	mountain	1.6×10^{-3}	~ 3	$\sim 1.5 \times 10^{-3}$
CHOOZ	300	cliff	2	$\sim 1.2 \times 10^3$	~ 0.3
Double Chooz near	60	mound	50	$\sim 1.3 \times 10^4$	~ 2
My Detector	0	N/A	110	??	$\sim 6 - 23$

Table 3.1: *Rates of neutron-causing processes observed at KamLAND and projected to proposed experimental sites*[40].

This increase in anti-neutrino flux and error elimination comes at a price however. By moving the near detector close to the reactor, this detector is moved closer to the surface of the earth. The earth serves as a good muon shield, and as seen earlier, muons are the source of much of the neutron delayed coincidence background. Previous neutrino experiments have thus been conducted deep underground to reduce as much as possible the muon flux.

An example of a neutrino experiment housed deep underground is KamLAND. Kam-

LAND eliminates backgrounds 1-3 above by applying a 2 ms cut after every muon that is detected either in the target volume or in the outer detector extending at least 3 m beyond the target volume in every direction. The ^{9}Li/^{8}He background is handled by applying two further cuts:

- A 2 second veto for events within 3 meters of a trackable but "non-showering" muon.
- A 2 second veto of the entire fiducial volume following an untrackable "showering" muon.

This approach works because KamLAND's target volume is large (13 meters in diameter) and the muon flux is low at its 1-km underground site ($\cong 1.6 \times 10^{-3}$ m^{-2}s^{-1}). No reactor-based θ_{13} experiment presently planned would have such a large target volume, and none could be so deep underground, since the goal is to be within about 200 meters of the reactor to keep the neutrino flux high for the near detector. In fact, Double Chooz's near detector is less than 2 meters radius in target volume and has a muon flux of $\cong 50$ m^{-2}s^{-1}. This high muon rate and small volume means that a track cut around a muon would effectively veto the detector almost all of the time.

New strategies are clearly needed to work in this environment. The first idea is to overwhelm the background with signal by moving the detector close to the source. Daya Bay and Double Chooz will use the strategy for the near detector. The Double Chooz near detector, for example, will be 400 meters from the reactors. At this distance the expected antineutrino event rate is 3000 per day while the ^{9}Li production rate has been projected to be 17 ± 3 per day[42]. The far detector is located 1.05 km away and is deeper in the ground. It features about 60 antineutrino events per day and 1.7 ± 0.3 ^{9}Li events per day. These estimates come from a scaling of measured ^{9}Li production cross-section with muon energy that is well motivated but has not been experimentally verified for ^{9}Li[43]. While this strategy will enable Double Chooz to significantly improve upon the CHOOZ measurement of θ_{13}, it is insufficient to reduce the total systematic uncertainties to the level required for a $\sin^2 2\theta_{13} < 0.01$ measurement.

Two further strategies might be helpful in dealing with ^{9}Li backgrounds. The muons can possibly be tracked more accurately. This would enable a much tighter cylinder cut to be made to passing muons. This of course assumes that ^{9}Li events are tightly correlated in space with the muon track, which has not been clearly shown. For a detector like Double Chooz, the size of the cylinder cut would need to be under 2 cm to keep the dead volume-time below 10%[44]. Obviously, this would require a relatively high accuracy of muon tracks and may be impractical for current neutrino detector designs. A final thought is to better study muon interaction by spallation with liquid scintillator to know when a muon is a "candidate" to produce ^{9}Li. This strategy would enable muon crossings that have a low probability of producing ^{9}Li to not be vetoed, and essentially ignored. If a very large fraction of muons fall into this category, then much of the detector live time can be maintained even in an environment of high muon flux. It has been suggested[44] that muons depositing minimum energy or muons that cross without producing neutrons may fit this condition. Other characteristics of muons that may be relevant include muon scattering angle, excess local energy deposit (indicating ^{9}Li production) or number of secondary tracks. To determine if this strategy is relevant more study of the ^{9}Li production mechanism will be necessary. That is the purpose of this present experiment.

Chapter 4

The Detector for the ^{9}Li Measurement

In an attempt to better understand the production of ^{9}Li in liquid scintillator by cosmic ray muons a low-cost detector has been designed specifically for this purpose.

4.1 Detecting ^{9}Li

Before discussing the detector a few words should be said about what the detector is looking for. ^{9}Li is relatively long-lived radioactive isotope with a half-life of 178.3 ms and a mass excess of 24.954 MeV[45]. ^{9}Li has several decay modes but 50.8% produce a β^- and neutron pair. The specific reaction is either

$$^9_3\mathrm{Li} \rightarrow \mathrm{e}^- + \mathrm{n} + \bar{\nu}_\mathrm{e} + ^8_4\mathrm{Be}, \tag{4.1}$$

where the ^{8}Be subsequently decays to 2 α's, or

$$^9_3\mathrm{Li} \rightarrow \mathrm{e}^- + \mathrm{n} + \bar{\nu}_\mathrm{e} + 2\alpha, \tag{4.2}$$

where the α's are created directly. The Q-value, or the total kinetic energy available for the decay components, is 11.94 MeV[46].

^{9}Li mimics a neutrino capture event because some relatively long time after it is created by a muon traversing a neutrino detector, it decays into a β electron and a neutron. Note that ^{8}Be has low kinetic energy, so it is not relevant for our purposes. The electron slows

down as it interacts electromagnetically with the liquid scintillator molecules in the detector, depositing energy that is emitted as photons by the liquid scintillator. Then, the neutron captures on something in the detector, for example hydrogen, gadolinium, or, in our case, chlorine. Once again the energy is converted into visible photons by the liquid scintillator. The photons from both interactions are measured by the PMTs to produce signals the detector records. This pair of signals is difficult to separate from the positron and neutron capture pair signals created in a genuine neutrino interaction.

This paper discusses a detector designed specifically to detect ^{9}Li by its related signals. One key element for such a detector that is worth mentioning here is what this detector uses to capture neutrons. There are many isotopes that one can use to capture neutrons. We want a capture agent with a relatively high thermal neutron capture cross-section so that as many of the neutrons as possible will be captured. We also want a capture agent that produces signals that are easy for the detector to measure. A common choice for many experiments that are deep underground is ^{1}H. Hydrogen has a thermal neutron capture cross-section that is respectable (about 300 mbarn). When combined with how abundant hydrogen is in water, a large tank filled with water becomes a good neutron detector. The main drawback is that the Q-value for neutron capture on ^{1}H is 2.2 MeV. This value is right in the middle of the gamma and neutron background energies seen at the earth's surface. Thus, hydrogen is not a good choice for a detector on or near the surface of the earth.

To get around this background problem many detectors employ gadolinium. Gadolinium has a natural composition thermal neutron capture cross-section of 49,700 barns. ^{157}Gd (15.7% natural abundance) has a thermal neutron capture cross-section of 254,000 barn. In addition, the Q-value is large, 7.9 MeV, and is emitted as a "fireball" of γ photons. This enormous capture cross-section combined with the γ "fireball" make Gadolinium the "ideal" thermal neutron capture agent for experimental use[46]. Unfortunately, Gadolinium can be somewhat difficult to work with, particularly when dissolved in liquid scintillator.

This experiment uses a compromise capture agent of ^{35}Cl. The thermal neutron capture

cross-section is 35.5 barn. The detector is constructed with PVC material, which is composed of a large amount of chlorine. The natural abundance of ^{35}Cl is 75.55%, so there is a lot of ^{35}Cl to capture on. The Q-value is 8.579 MeV, and is emitted as photons directly[46]:

$$n + {}^{35}\mathrm{Cl} \rightarrow {}^{36}\mathrm{Cl} + \gamma\text{'s}. \tag{4.3}$$

4.2 Detector Design

The detector itself consists of seven rectangular box-shaped layers of liquid scintillator, each with interior box dimensions of 125 cm $\times$ 75 cm $\times$ 10 cm. The boxes are made of white PVC (poly-vinyl chloride).

The small ends of each layer feature two Hamamatsu R2154-05 photomultiplier tubes (PMT) mounted in clear acrylic window ports for gathering the photons emitted by the liquid scintillator. The white PVC features high reflectivity that enables a large fraction of the light generated anywhere in the box to be collected by one of the PMTs. The liquid scintillator fluid level was also set to just below the top so that there is total internal reflection for the appropriate range of incident angles.

The outputs of the two PMTs on each end are combined into one signal, and then the two signals for each layer are input into the channel A and channel B inputs respectively of a Pico Technology Limited PicoScope 3205 PC oscilloscope. Seven oscilloscopes are utilized to record all the signals from the detector. Triggering on each scope is handled by an external trigger from the data acquisition system (DAQ) that will be described below.

The detector is then surrounded with 2 inches of 5% Boron loaded polyethylene plastic. Boron serves as an effective thermal neutron capture agent (about 10 attenuation lengths at this concentration). Thermal neutrons coming from outside the detector will be attenuated. In addition, any fast neutrons thermalized by the shielding should be captured as well. This effectively isolates the detector from thermal neutrons created outside the detector itself. Neutrons captured in the detector should then be those emitted by ^{9}Li decay.

4.3 Triggering

4.3.1 Overview

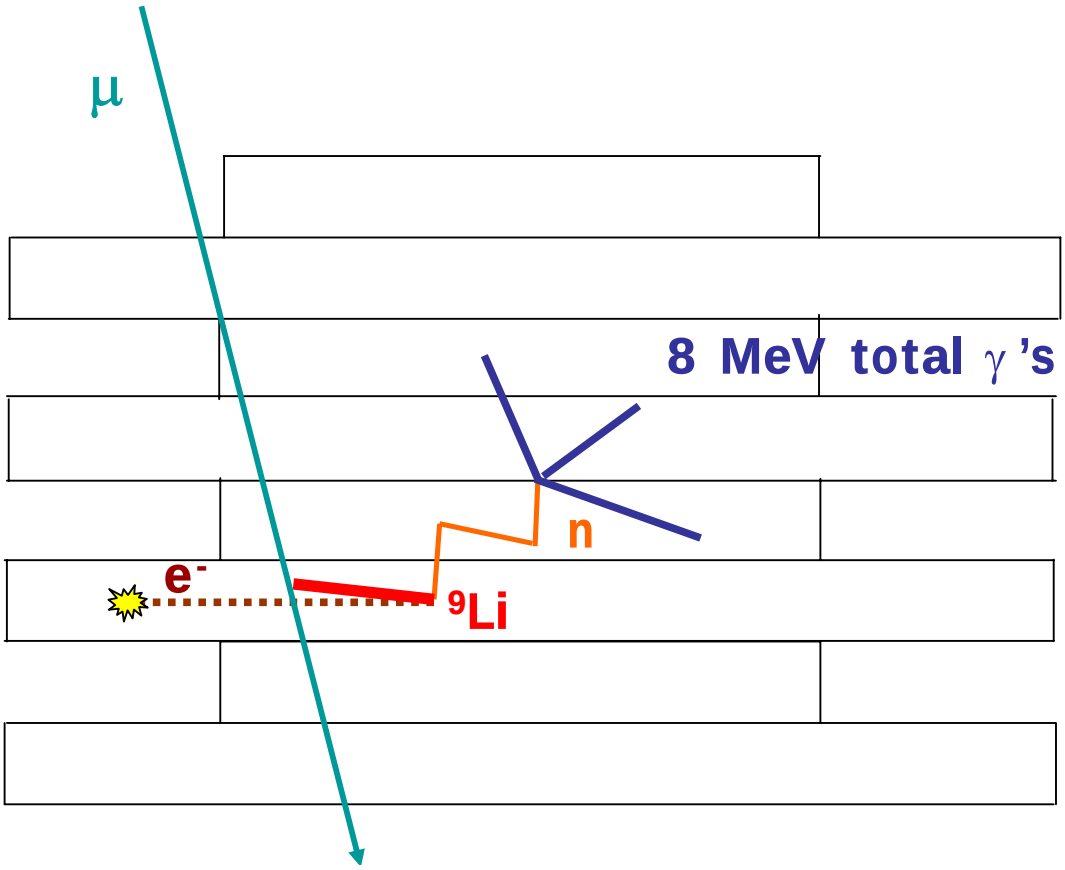

Figure 4.1: *A cartoon of* ^{9}Li *interaction in the detector. Note that the muon passes through the complete detector. The* ^{9}Li *stays in the same layer it was created, and then it decays. The electron deposits energy in the layer in which it is created, providing a prompt signal. Meanwhile, the neutron travels through the detector until it is thermalized and captured on* ^{35}Cl*. The resulting excited state of* ^{36}Cl *deexcites, emitting several* γ*'s that potentially triggers several layers in the detector.*

Given the fact that the vertical muon rate is rather high at the Earth's surface ($\approx$ 70 $\mathrm{m^{-2}s^{-1}sr^{-1}}$ for muons with momentum greater than 1 GeV/c) a robust triggering system is necessary to reduce random coincidences[29]. As a guide, let us assume the detector sees a solid angle of about 1.6 sr. This corresponds to accepting muons within about 42 degrees of vertical. The muon rate is then $\approx$ 110 $\mathrm{m^{-2}s^{-1}}$. Keeping in mind that the vertical cross-

section of a layer in the detector is 0.9375 m^2, and that we are looking for two signals in 200 μs, the rate of double coincidence for background muons is then:

$$\text{MuonBGRate} = (110\ \text{m}^{-2}\text{s}^{-1})^2(0.9375\ \text{m}^2)^2(200 \times 10^{-6}\text{s}) = 2.12\ \text{s}^{-1} \tag{4.4}$$

This double coincidence rate is greatly reduced from the singles rate, but is still too high. Muons deposit energy in scintillator at about 2 MeV per cm traversed. Each layer is 10 cm thick, so a vertical muon will deposit around 20 MeV per layer. Muons away from vertical will have a spectrum of energy depositions based on how far they travel in a given layer. In general, they travel more than 10 cm in a layer, so their energy deposit is greater than 20 MeV. Therefore, a hardware cut is applied that rejects prompt signals that are too large. (To be clear, this cut is on the detector sum channel. This channel is the simultaneous sum of all seven layers, and is divided by "about" 13 times. If the signal on this channel exceeds -30 mV in amplitude, it is an unacceptable prompt signal. The exact corresponding energy value this represents is unknown, but, looking at data, it is clearly greater than 20 MeV.) Using this prompt veto dramatically reduces the observed background rate to about 0.3 Hz.

Further hardware cuts are needed to reduce non-muon background. Accidental backgrounds are controlled by requiring the prompt and delayed signal to be at least -30 mV in amplitude. There are also topological cuts. A "real" ^{9}Li event will appear as a prompt in one layer, and then a neutron-like event of a total of $\sim$9 MeV in multiple layers within the 200 μs coincidence window (see Figure 4.1). As a result, the prompt signal is required to be only in one layer, and the delayed signal must be in at least two layers. These conditions are required for the data for a given event to be recorded by the DAQ system. Note that these hardware cuts are fairly loose. The idea is to limit as much as possible the unwanted signals in the detector while not eliminating any of the ones we want. To facilitate this we keep the hardware cuts loose while recording data, and then apply stricter requirements with off-line data processing.

4.3.2 Electronics

We will next detail the trigger system itself. Figure 4.2 sketches the trigger electronics. The purpose of the trigger electronics is to decide what signals meet the criteria that have been established, namely that a single layer signal is followed within 200 μs by a multiple layer signal that is not too big. Signal pairs that meet these conditions trigger the electronics to send a signal to the computers to record the waveforms present on the oscilloscopes for the last 200 μs.

Each layer of the detector has signal from two ends, A and B, each formed from the output of two PMTs. Each end first is connected to an RC circuit made of a 51-Ohm resistor and a 1000 pF capacitor. The purpose of this small circuit is to expand the fast signal output of the PMTs, extending it in time. After the RC circuit, each end is placed into one channel of a Phillips Scientific Model 776 sixteen channel amplifier where the signal is amplified (exact value was not measured). Each channel has two outputs. One channel goes directly to the appropriate oscilloscope in preparation for data recording. The other output is used for further trigger decision making.

After the amplifier, the two channels from each layer are combined into one signal. The two channels of layer seven, six, five, and four are each combined via a Lecroy 428F linear fan-in/fan-out. The two channels of layers three, two and one are each combined with a custom made "super" fan-in/fan-out that was obtained from the old CHOOZ experiment. (Note there is no reason for there being two different combining electronics except for equipment availability) There is no gain in this combination process.

Following combination, each layer is connected to a CF8000 octal constant fraction discriminator (CFD). The purpose of the CFD is to take advantage of two logic outputs of this device. First, a multiplicity output provides a signal whose amplitude discretely corresponds to the number of inputs (layers) that have a signal above a threshold (set to minimum in this case). If one layer meets this threshold requirement, the output is -100 mV (Note: there is no connection between this voltage and the voltage of the actual signal

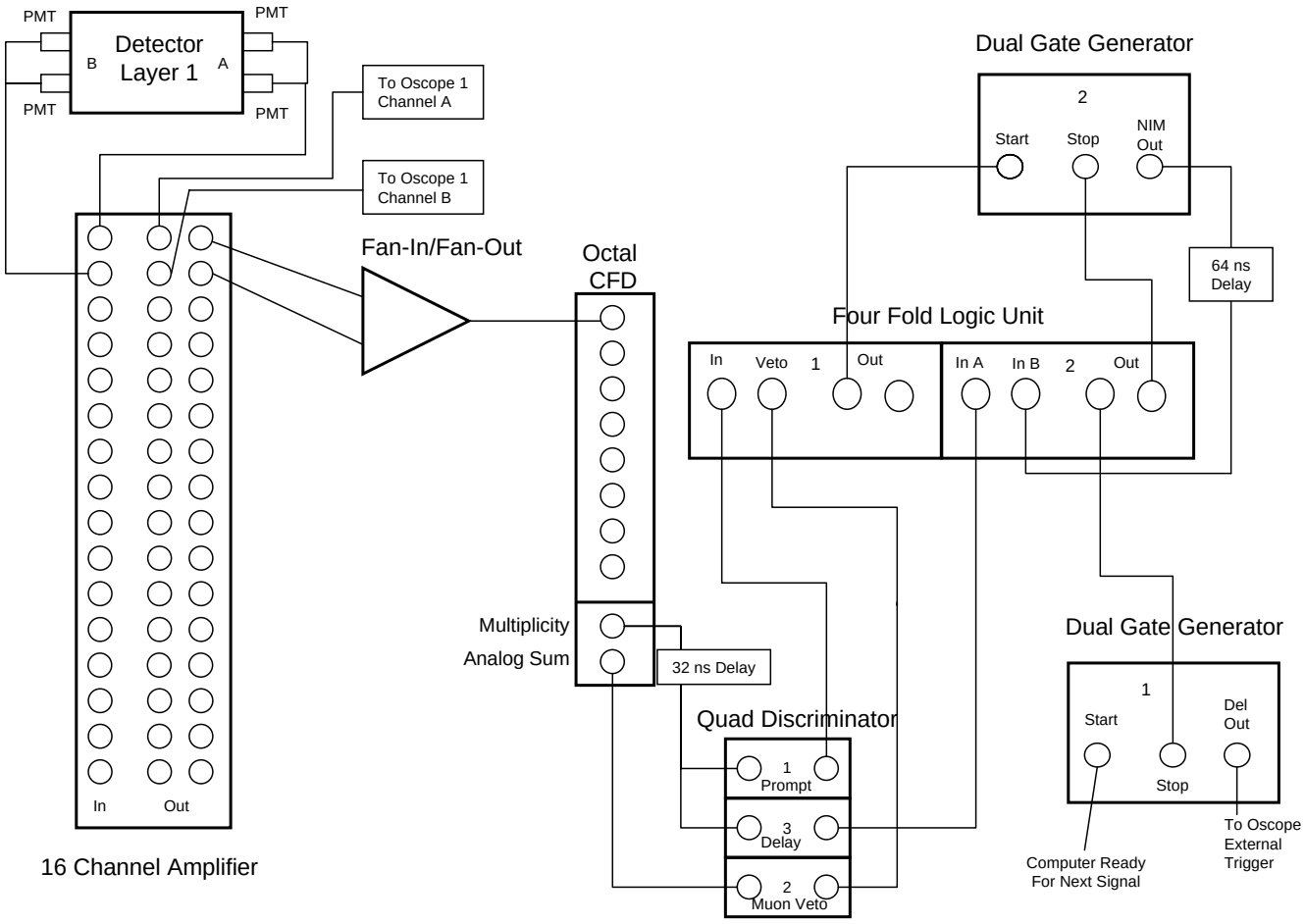

Figure 4.2: *A schematic diagram of the triggering system. For simplicity only one layer's input into the 16 channel amplifier and octal CFD is shown.*

present in the box. This level simply indicates the number of layers that have a signal that meets the threshold requirement.). If two layers have such a signal, -200 mV, and so on up to a maximum of four layers with a -400 mV output. Secondly, there is an analog sum output of all channels connected to the CFD. The output is divided about 13 times.

The multiplicity output of the CFD is connected via a delay of 32 ns to one section of a Lecroy Model 821 Quad discriminator. First, a signal is analyzed to see if it is a prompt

signal. A proper prompt is in a single layer, so the threshold of the discriminator is set for one layer (-100 mV) from the CFD. If this criterion is met, a standard signal is output. The sum output of the CFD is simultaneously analyzed by the second section of the Lecroy Model 821 to make sure it is not too large. A real prompt will correspond to less than 20 MeV in energy, but this requirement is difficult to introduce at this stage. Instead, the threshold of the discriminator is set to trigger if the detector sum signal (which gets divided about thirteen times) is larger than -30 mV in amplitude. This threshold effectively eliminates prompt signals that are too large. The output of the prompt candidate and the veto signal are both connected to a Lecroy Model 365AL 4-fold logic unit. If the prompt signal itself is also less than -30 mV in amplitude, an output signal is generated.

For a proper prompt candidate, the output is sent to the start input of a Lecroy Model 222 Dual Gate Generator set to a 200 μs time window. If a second signal is input within 200 μs a negative NIM signal is generated. A proper second signal is a delayed signal candidate. A delayed signal candidate is determined by sending the same multiplicity output of the CFD to the third section of the Lecroy Model 821 Quad discriminator. This time the signal needs to be in at least two layers of the detector. If this threshold is met, a standard signal is output to different section of the Model 365AL 4-fold logic unit. Also, if two signals were found within the 200 μs time window, a signal was generated and sent to this logic unit. If both conditions are true, a proper delayed-coincidence signal candidate has been found. A trigger signal is then generated and sent to the oscilloscopes where the previous 200 μs of data is recorded for all 8 oscilloscopes (seven layers and the detector sum monitor).

4.4 Liquid Scintillator

The discussion about the detector can't conclude without mention of the most important, but often neglected, component of this detector, the liquid scintillator. Scintillation is the process whereby an ionizing particle traversing matter excites the molecules of the medium it travels through. Certain types of molecules release a small fraction of this energy as optical

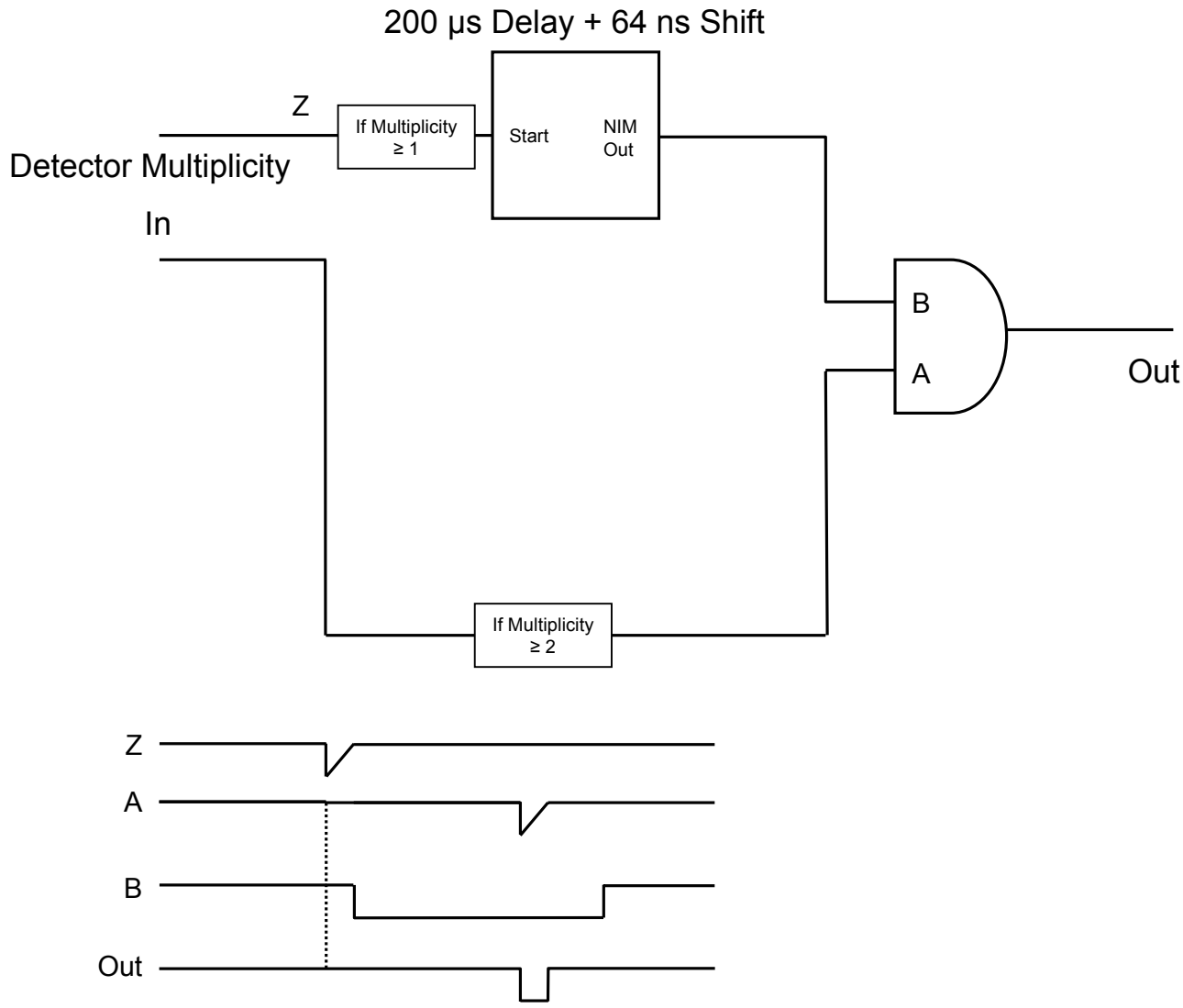

Figure 4.3: *A diagram of the 200 μs time window for double coincidence of signals meeting the proper criteria. The prompt signal must have at least multiplicity (number of layers with a signal) one, and the delay signal must have at least multiplicity two. The out signal shown is used to trigger the oscilloscopes for data acquisition.*

photons (around 3% of the energy), especially organic molecules[29]. The scintillator this detector uses is Bicron 517L. The Bicron 517L is mineral oil with about 20% pseudocumene (1,2,4-trimethylbenzene) dissolved in it as the main scintillator component. There are also wavelength shifters included to increase the wavelength of the scintillation light into the visible region. Bicron 517L's emission spectrum peaks at 425 nm, so the energy of a typical optical photon produced by the liquid scintillator is 2.9 eV[47].

In real scintillator the scintillation light emitted for energy deposited by a particle traveling a distance dx is not quite proportional to the energy deposited, dE. Instead, the scintillation light dS follows the empirical Birks' law:

$$dS = k\frac{dE}{1 + k_B\frac{dE}{dx}} \tag{4.5}$$

where k is some proportionality constant and k_B is Birks' constant for the scintillator in question. The quenched energy seen may be defined as

$$dE_{Quenched} = \frac{dE}{1 + k_B\frac{dE}{dx}}. \tag{4.6}$$

Chapter 5

Off-line Data Processing

The data acquisition system records every event that triggers the hardware. As is often the case in experiments, most of these triggers are for things that are not of real "interest" to us in finding ^{9}Li. Despite the signal thresholds and hardware "muon" veto, many "false" single-layer signals start the delayed coincidence process, and many muons that do not deposit an overly large amount of energy still pass through. Therefore, an off-line process has been developed to sort through the raw data to find events of interest. This process is all done with software after the data has been recorded, and involves four levels of data processing.

The basic idea is as follows (see Figure 5.1). The data for each event is recorded separately for each channel of the detector (Recall there are two channels per layer, and seven layers.). We are looking for a single-layer signal followed by a multiple-layer signal within 200 μs. So, the data must be scanned to look for this coincidence of signals. First, the data for a given event is scanned to find all of the peaks on each channel. Second, the peak data for that event is scanned to find all of the single-layer peaks and all of the multiple-layer peaks. Third, these single-layer and multiple-layer signals are compared to see which ones match the criteria of a coincident signal candidate. Steps one through three are repeated for each event. Finally, those coincident signals from all of the events that meet the requirements are then converted into the appropriate format for further analysis.

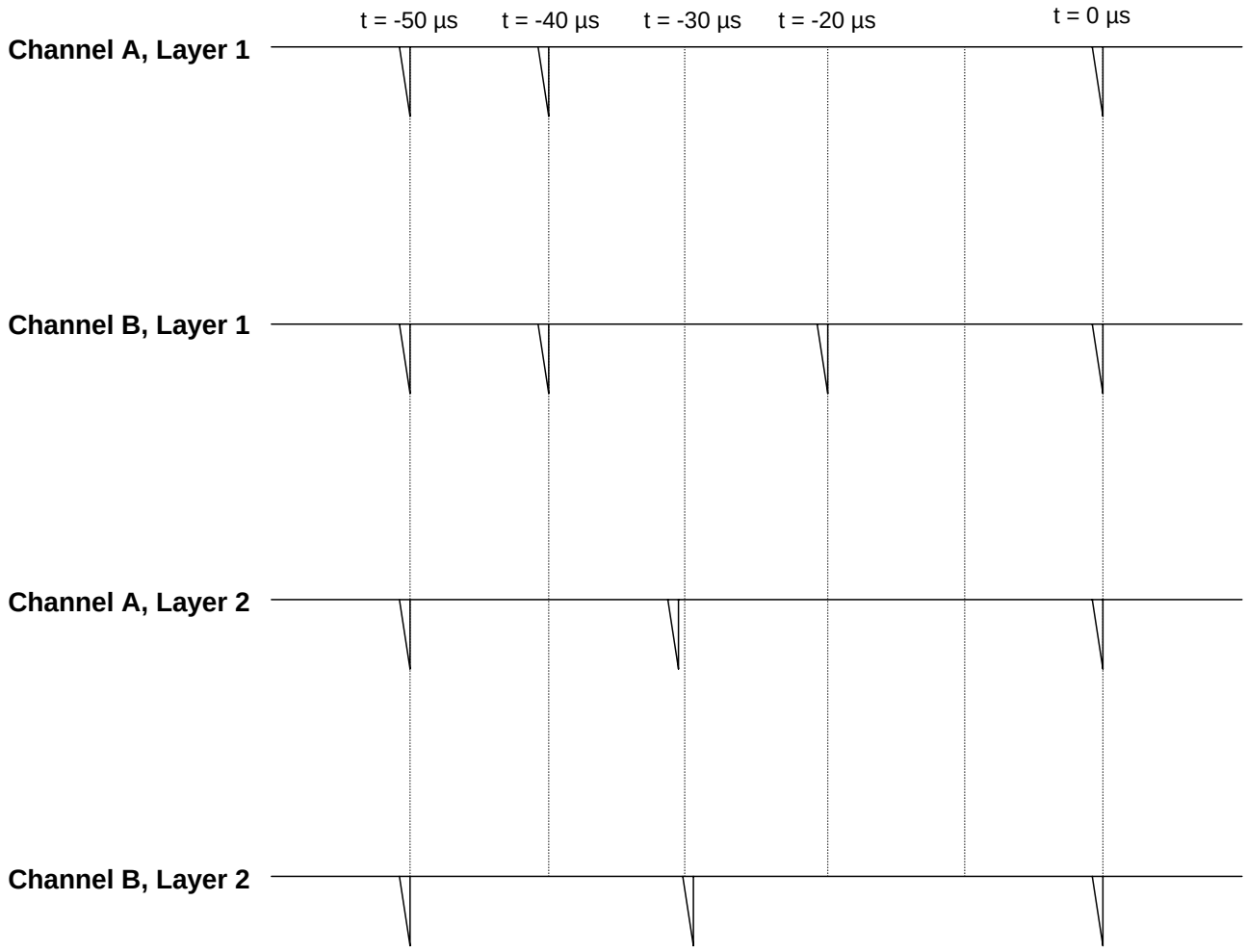

Figure 5.1: *A simplified example of the data processing procedure. Shown are two layers with their respective simplified channel waveforms. The level one process searches each channel to find all of the peaks and reports the time position and the integration of the area under the curve. Level two compares the peak locations on each channel to find single-layer pulses and multiple-layer pulses. In this case, level two would find a single-layer pulse on layer one at t = -40 µs and a single-layer pulse on layer two at t = -30 µs. Notice channel B, layer 1 has a signal at t = -20 µs that has no corresponding signal on any other channel. It is therefore ignored. Level two processing would also find two multiple-layer signals, one at t = -50 µs and the other at t = 0 µs. The level three output of this data would be the information for the coincident pair of the single-layer signal at t = -40 µs and the multiple-layer signal at t = 0µs, and the coincident pair with single-layer signal at t = -30 µs and the multiple-layer signal at t = 0 µs. The multiple-layer signal at t = -50 µs would be ignored.*

5.1 Level One: Peak Finding

The initial process is to find all of the signal peaks for each event. Recall that the actual data recording is performed by oscilloscopes connected to computers, with each layer of the detector having a separate oscilloscope assigned to it. Each side of a layer is then connected to one channel of the oscilloscope. Further recall that the oscilloscope samples every 10 ns, and we are interested in a 200 μs time window, so there are at least 20,000 data points involved for each channel for each event. For each data point, the time (in picoseconds) and amplitude (in mV) are recorded. An example of a typical event waveform from one channel is shown in figure 5.2.

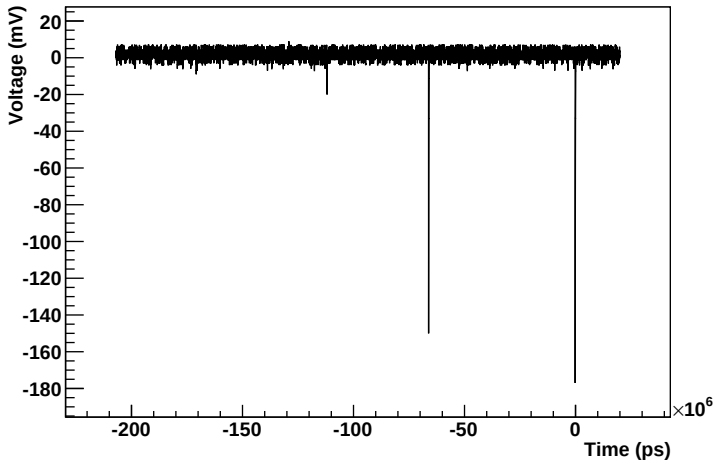

Figure 5.2: *A typical event waveform pattern for one channel taken by the PicoScope oscilloscope. Note time is in picoseconds.*

Examining figure 5.2, we see several interesting features. First, there seem to be three significant signal peaks. One is near time 0 s. Another is at time -65×10^6ps (-65 μs), and a smaller one is near -110 μs. In addition, there is a fairly noisy baseline at about 0 mV whose amplitude swings over at least 10 mV. Finally, note the actual recorded time window is greater than 200 μs. The time window is 230 μs, with 20 μs recorded after the trigger (these are the positive times), and 210 μs before the trigger.

Now, our ideal model was that an event should appear as a single-layer signal followed by a multiple-layer signal within 200 μs. Unfortunately, data collection in the real detector clouds this ideal picture. Data is recorded for each channel, with two channels per layer. To get an idea of what happened in each layer and in the full detector, all of the channels must synthesized and compared to discover what signals are single-layer, multiple-layer, or neither.

To keep the analysis simple, we are interested in finding all of the peaks on each channel for a given event, and keeping those peaks in time order. Time order is important because more than two signals often appear within the 200 μs time window, as we see in figure 5.2. At this stage, we will not be concerned about anything except to identify all of the signals with their event number, their location in time, the channel they occur on, and the integrated sum of the area under the peak in units of mV·ns.

To get a better handle on how this is done let us take a closer look at the peak near 0 s (see figure 5.3).

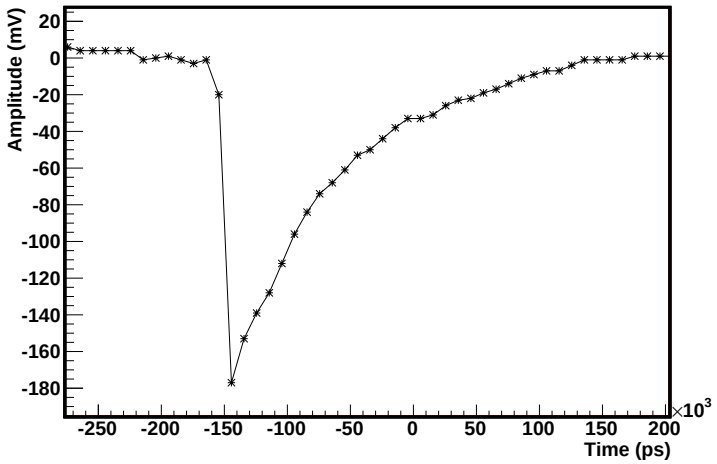

Figure 5.3: *A close up look at one peak from figure 5.2.*

Each star is a data point. The first step in finding a peak is to check the slope of the data point with the point before it. If the slope is more negative than -1.0 mV/ns (angle

more negative than -45 degrees), then a peak has been found. The next data point is then read in, and a running sum of the amplitude times the time step of 10 ns is started. This continues until the slope changes to 0 or greater. This point is considered the actual peak location, and the time is noted as the peak location. The peak integration continues until the signal returns to a predetermined fraction of the amplitude baseline. At this point, the peak is considered done, and the information of event number, channel, integration sum, and peak location is written to an output file.

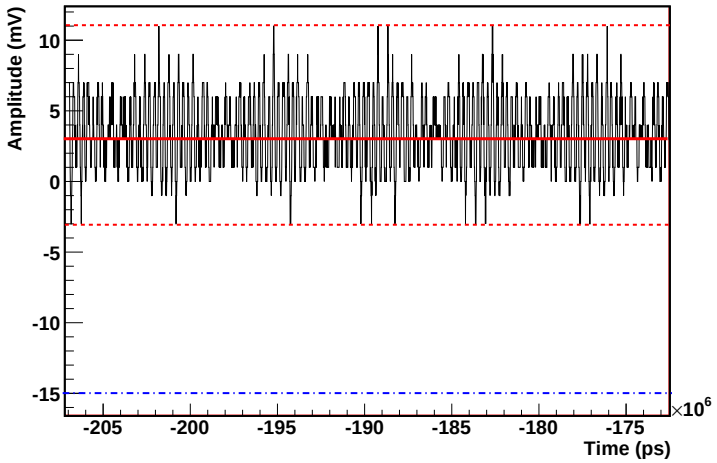

Figure 5.4: *A look at the variability of the baseline of the typical waveform. The solid line represents the average of the baseline. Level One finds the range of the variability, represented by the dotted lines, and then requires a peak to go beneath the dot-dash line, or three times the distance from the dotted lines to the baseline.*

There are of course complications to this basic idea. Some oscilloscopes are not centered at 0 mV for a baseline voltage, but are at some constant positive or negative DC level. The 10 μs of data before the 200 μs time window starts is used to measure what this baseline is. All subsequent amplitude measurements are made relative to this measured baseline.

As noted before, there can be quite a bit of variability around the baseline of the waveform even with no signal present. This variability can sometimes trick the peak-finding procedure detailed above into thinking that many peaks are present when there are in fact none (see

figure 5.4). The first obvious choice to correct this is to require the slope condition to be something more negative than -1.0 mV/ns. Unfortunately, doing so can cause some true signals to be ignored. The chosen solution is to measure what the typical amplitude variation is in the baseline in the time before -200 μs, and to require a peak to be greater than 3 times that variability from the baseline.

5.2 Level Two: Identification of Singles and Multiples

The output of level one processing is a file listing all of the peaks for a given event along with the channel, integrated sum, and the time position. In fact, there are two files with this information, since the DAQ system is split into two halves. One computer records layers 7 through 4, and a second records layers 3 through 0. Level two processing has the task of reading in these two files simultaneously, identifying single-layer signals, and signals that occur in multiple layers. To accomplish this task, there are two versions of the level two processing, one to report the singles, and a second to report the multiples. Please refer to figure 5.1 for an illustration of the data processing procedure that follows.

The first step in finding the single-layer pulses is to read the data in from the output files from level one. In one sense, this is trivial, but a critical step is performed here. At this point, the data for the integrated sum is in terms of the area under the curve in units of mV $\cdot$ ns. These units are not practical for further use, but we know this area is related to the energy deposited in the layer. Chapter Six describes how calibration factors are determined to convert this area to units of energy in MeV. As the values of the peak sum are read in, the calibration factor for that channel is used to convert the sum to an energy value.

For each event, each peak is read in one at a time. Peaks within 100 ns (or 100,000 ps) are considered simultaneous. If a signal is found to appear simultaneously in more than one layer, it is a multiple-layer signal, and this program ignores them. If both channels in a layer have a signal present simultaneously, then this is judged to be a legitimate single-layer pulse and the total layer energy, the time, the layer number, the separate channel energies,

and the detector sum from the CFD output (contained in the layer 0 channel B output) are written to an output file containing all of the singles candidates.

A similar process is followed for the multiple-layer pulses in a separate program. If a signal is found to be simultaneous in multiple layers, then the number of layers in which both channels for that layer have a simultaneous signal are counted and recorded as N_m. The following data for that signal is then output to a file containing all multiple-layer signals: event number, total signal energy, time, the energy for each of the channels in the whole detector, and N_m.

5.3 Level Three: Matching

Our ideal event would be a single-layer pulse followed by a multiple-layer pulse within the 200 μs time window. We now have the data in two separate files. One contains the single-layer signals, and the other the multiple-layer signals. Thus, we want to pair together all relevant singles in an event with the appropriate multiple-layer single in that event. The electronics are set so that either a single-layer pulse or a multiple-layer pulse can initiate the DAQ system, but only a multiple-layer pulse after the initial signal can trigger the data collection of an event. Hence, level three requires the signal near time 0 s (actually from -250,000 ps to 0 ps) to be a multiple-layer pulse, and it ignores all other multiple-layer pulses.

Remember that when the data collection is triggered, it records everything in the oscilloscope's buffer for the last 200 μs, including the prompt that started the double coincidence clock, any singles that came in after that, and if there is any time left, data from even before the double coincidence clock was triggered. There are thus many signals in the event waveforms that are of no interest to us. In particular, an event can have extra single-layer events. The difficulty is there is no readily apparent way to identify the unwanted single-layer signals. So, all single-layer signals for an event are matched with the multiple-layer signal near zero.

The layer three program then pairs all singles the multiple-layer signal that closed the DAQ clock and triggered data recording. All of these pairs are written to an output file containing all of the information for the single and multiple-layer signals: time for each signal, integrated sum of each signal, layer of the single, channel breakdown of energy for the multiple-layer signal, and the number of layers that the multiple-layer signal was present on.

This final output file is then read into the ROOT data analysis system (step four) for data analysis.

Chapter 6

Calibration

"A false balance is abomination to the LORD: but a just weight is a delight."

—Proverbs 11:1

From ancient times, a proper calibration of devices used to measure has been insisted upon. This is no less true in science today. Essentially, all this detector does is capture photons created inside of it. From these photons, all other information is extracted, in particular, energy. Therefore, it is critical to know how much energy a captured photon has. The process of determining how much energy is deposited in the detector is calibrating the detector.

6.1 PMT Voltage Determination

The principle that allows the photomultiplier tube to work is the photoelectric effect. A photon of sufficient wavelength incident upon the treated glass surface ejects an electron. That photoelectron is then guided by electric fields in the tube to strike a metal plate known as a dynode. More electrons are ejected because of this interaction. These electrons are then guided through multiple dynode layers, creating more and more electrons with each interaction with a dynode, until the small energy of the incident photon has become a measurable current. This current is then measured across a load to produce a signal in an oscilloscope.

Many factors determine how much gain there is from the incoming photon to the resulting output current. A key one is the high voltage applied to the PMT. This voltage is divided up across the dynodes with the effect that more voltage at the dynodes means that the incident electrons produce more ejected electrons, and hence a greater signal.

The initial calibration of the detector consisted of finding the voltage level that roughly gave all PMTs the same gain. Note that it is necessary for all PMTs to have roughly the same gain so that without bias signals of the same amplitude are accepted by all channels in the detector. This calibration was rough, however, since the voltage divider being used to provide power to the PMTs is restricted to 50 V steps, and a 300 V variance voltage range. Due to power supply current limitation it was decided to have the maximum PMT voltage be 1600 V.

The basic PMT voltage selection is modeled from a report by A. de Capoa[48]. A previously constructed dark box was set up with a green LED and a stand for a PMT. The voltage supplied to the LED was set to a +5.0 V level and an on-time of different amounts from 15ns to 30ns in 5ns steps, supplying varying amounts of weak light with the changing width (Note at this signal strength the LED still appeared "off" to the human eye). The PMT signal was then recorded for a large amount of triggers and various PMT voltages. The area of the pulse was then determined and reported. In addition, a similar procedure was performed with the box dark (LED off) to measure the background, and an average dark signal was determined. This average dark signal was subtracted from the LED result for each instance, and the resulting area was plotted as a histogram. A Gaussian distribution was fit to this histogram. From this Gaussian fit a factor K' was measured,

$$K' = \frac{\mu}{\sigma}. \tag{6.1}$$

This factor K' is related to the ratio of the photoelectrons incident to the PMT and the resulting ADC count of the PMT output, but it is a relative factor and not a true measure of the absolute number of photoelectrons per ADC count. Note that we are in no way attempting an absolute calibration of ADC count per photoelectron, but we are instead

looking for a relative measure of the gain each PMT has for similar light level inputs.

Inverting this factor, we find a new factor K that tells us something about the ADC count per incident photoelectron. Again this is a relative factor. A K factor equal to 10 was chosen as an arbitrary calibrating point after measuring several PMTs. The PMT voltage selected for each PMT is the one that had a average K factor closest to 10, recalling that the voltage divider was limited to 50 V steps. All PMTs selected have a "calibrated" operating voltage between 1300 V and 1600 V.

6.2 Calibration of Channels

In addition to the gain of the PMTs, the sixteen-channel amplifier amplifies each channel by some unknown factor. These two gains can be accommodated readily by taking a signal of known energy and matching it to the output of a channel in the detector. A conversion factor between ADC count and energy is then found and applied to all the data. This process assumes that the detector behaves in a linear fashion, so that matching the energy to ADC output at some point effectively calibrates the system through all its range.

6.2.1 Calibration Process

The calibration of this detector depends upon the fact that muons are known to deposit energy in liquid scintillator at approximately 2 MeV per cm traveled through. Each layer of the detector is 10cm in height, so a vertical muon will deposit 20 MeV in each layer. Muons that come in at a shallower angle will generally travel farther in each layer, depositing more energy. This means that each separate layer can be calibrated independently. A further assumption for calibration is that vertical muons that fully trigger the detector travel through the fiducial volume of the detector, and that each side of each layer sees one-half of the signal, or 10 MeV.

The energy loss of a charged particle passing through a "thin" layer of matter is well

described by the Landau distribution:

$$p(x) = \frac{1}{\pi} \int_0^\infty e^{-t \ln t - xt} \sin(\pi t) dt \tag{6.2}$$

This distribution has two parameters, the most-probable-value (mpv) and σ. The mpv term is the most probable value of the distribution, while sigma is a scale parameter that relates to the width of the distribution. A characteristic of the Landau distribution is that for mpv = 0 and $\sigma = 1$, the maximum of the distribution is at -0.22278. Thus, for values other than the above:

$$\text{Peak} = \text{mpv} - 0.22278\sigma. \tag{6.3}$$

To accomplish this calibration, the hardware "muon" veto is disabled, so that large signals are allowed to trigger the detector. Doing so causes a complication however. The detector operates with the oscilloscopes set to 200 mV maximum. Large signals like vertical muons will easily put the oscilloscope to full scale, heavily truncating the signal by cutting it off. The result is that the integration of the charge deposited will be artificially low for large signals. This causes the distribution seen by the detector to deviate from Landau for large signals. Still, the calibration can be accomplished by only fitting the lower end of the vertical muon distribution, especially the peak.

To complete this phase of the calibration the peak found for each channel is compared to 10 MeV worth of energy. The conversion factor is then $\frac{10 \text{ MeV}}{\text{Peak(in mV·ns)}}$ for each channel. This factor is applied to the data at level two of data processing, and ADC counts are converted to MeV. Table 6.1 details the results of the calibration for each channel.

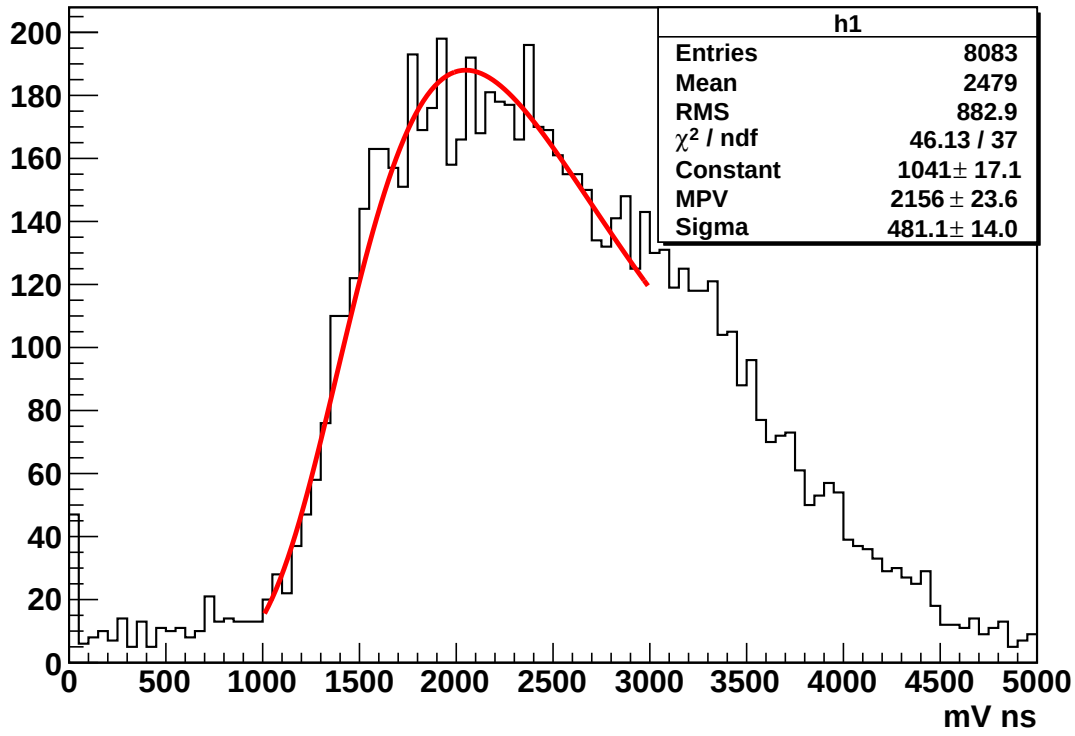

Figure 6.1: *The Landau function fit for channel A layer 7.*

Channel(side layer)	Peak(mV·ns)	Constant	MPV(mV·ns)	σ(mV·ns)
A7	2115.020	1055 ± 18.7	2231 ± 28.6	520.6 ± 22.0
B7	1889.070	1072 ± 18.3	1994 ± 25.7	471.0 ± 16.6
A6	1392.722	1313 ± 24.2	1468 ± 19.8	337.9 ± 13.0
B6	1156.997	1530 ± 28.6	1220 ± 21.6	282.8 ± 13.3
A5	2155.180	1091 ± 16.9	2296 ± 37.7	632.1 ± 26.9
B5	2377.871	1046 ± 16.4	2527 ± 54.1	669.4 ± 35.9
A4	1539.967	1319 ± 21.6	1633 ± 23.8	417.6 ± 15.1
B4	548.579	3065 ± 53.6	583.4 ± 5.6	156.3 ± 4.0
A3	723.941	2424 ± 43.6	769.5 ± 8.6	204.5 ± 6.3
B3	849.020	2187 ± 43.9	898.5 ± 8.4	222.2 ± 8.6
A2	761.929	2044 ± 38.4	807.8 ± 9.7	205.9 ± 6.5
B2	599.054	2533 ± 45.5	639.4 ± 6.1	181.1 ± 4.4
A1	1413.938	1157 ± 23.4	1483 ± 18.5	310.1 ± 12.0
B1	2363.334	1028 ± 18.5	2487 ± 25.4	555.1 ± 22.0

Table 6.1: *Summary of Landau distribution fit to detector channels.*

Chapter 7

Radioactive Source, Efficiencies and Background

This chapter deals with a hodgepodge of things that haven't been discussed yet. As part of bringing this detector online, a radioactive source was used to provide signals similar to those ^{9}Li produces, only at a higher rate so the detector response can be checked thoroughly. The efficiency of the detector to measure these signals can then be determined. Finally, the background signals that come along with the ^{9}Li signal are measured.

7.1 Radioactive Source: AmBe

Part of the detector commissioning process involves showing that the detector can identify the real signals it will be looking for. ^{9}Li decays into a β electron as a prompt and a neutron which eventually is captured and provides the delayed signal. To mimic this pair of signals in the detector a radioactive source was utilized. $^{241}_{95}$Am/Be (Americium-Beryllium, call it AmBe for short) is a neutron emitter in the 4 to 8 MeV range, which is realistic for ^{9}Li. Also, AmBe emits gammas with energy of 4.43 MeV. This gamma substitutes for the ^{9}Li β electron which has an energy spectrum from 0 to around 11 MeV, peaking at 6 MeV.

The AmBe source that was utilized was a pretty active one. As an α emitter, the AmBe source has 110 mCurie decays (4.07x10^{9} decays/sec). For every decay, an ideal AmBe source emits 6x10^{-5} neutrons and 4x10^{-5} γ's, resulting in about 250,000 pairs per second. This

high rate of neutrons and γ's dramatically increased the observed trigger rate of the detector. The background rate, as stated earlier, is about 0.3 Hz in normal operation mode (i.e. with prompt "muon" veto, signal threshold, and multiplicity requirements). With the source deployed 350mm above center of the top of the detector, the rate was about 13 Hz.

Looking at the results shows the effectiveness of the detector. Figure 7.1 shows a plot of the raw delayed signal. The large feature is the muon spectrum. Note that there is a distinct peak from 0 to 10 MeV. This is the neutron capture signal.

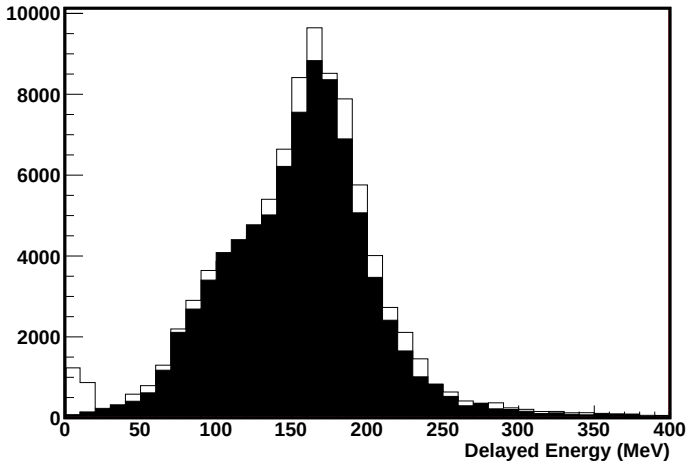

Figure 7.1: *A plot of the delayed signal energy with the AmBe source (white) and background only (black). This is a raw plot with no cuts. Notice the signal in the 0-10 MeV range. This is the neutron capture signal. The large signal above 50 MeV is the muon energy spectrum.*

Next, Figure 7.2 shows the delayed signal in the range we expect the neutron capture signal for both AmBe source data and background data. Here we also apply the standard signal cuts: prompt energy > 3 MeV and layer-multiplicity for the delayed signal of 2 or 3.

Figure 7.3 takes a look at the prompt energy spectrum just for the AmBe source. Compare with Figure 7.12 to see what the background looks like with no AmBe source signal.

Finally, Figure 7.4 shows the time difference between the prompt and the delay signal. It is clearly flat, which is consistent with Monte Carlo results for this Δt (The Monte Carlo

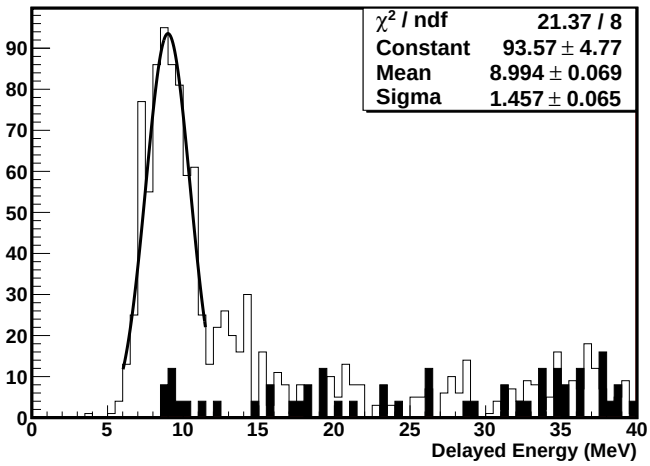

Figure 7.2: *A close view of the neutron peak from AmBe source data (white) and background only data (black), with a Gaussian fit. The energy release for ^{36}Cl is 8.579 MeV. The fit here yields 8.994 MeV. Cuts for this plot are the standard signal cuts: prompt energy > 3 MeV and delayed signal layer-multiplicity 2 or 3.*

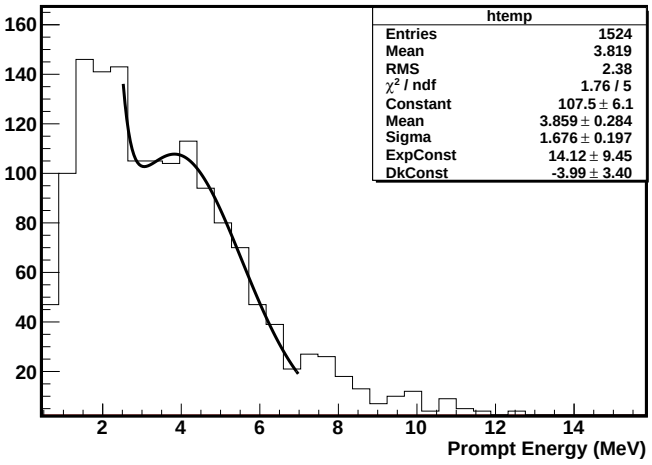

Figure 7.3: *The prompt energy spectrum with the AmBe source. Full signal cuts are applied here with delayed energy greater than 3 MeV and less than 20 MeV, and a delayed signal layer-multiplicity of 2 or 3. Fit is for a Gaussian plus an exponential distribution.*

simulations will be discussed in section 7.2).

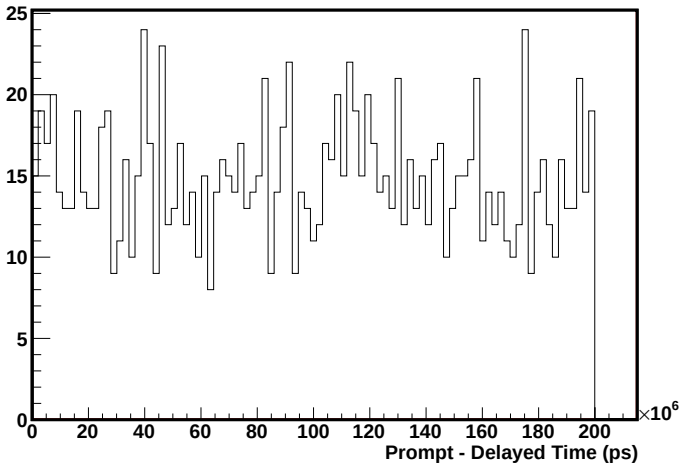

Figure 7.4: *Time difference between prompt and delayed signal with the AmBe source and full signal cuts applied. The distribution is flat, which is consistent with the Monte Carlo results which were flat up to 200 μs.*

7.2 Efficiencies

Another part of the detector commissioning process is to determine the ability of the detector to actually detect what you want it to. The measure of this is called the efficiency of the detector. It is important to remember that real detectors are incapable of detecting perfectly every event it is designed to measure. There are many effects that cause this. The devices making up the detector may misfire and create "fake" signals, or they may miss a real event. Particles, such as β electrons in this experiment, may have energies too low to be measured or below some hardware threshold. The hardware and software takes time to record what has happened, and events that transpire during that time may be lost. Even if every device worked perfectly, the detector has a geometry that limits how well it can measure.

In this experiment there are at least two efficiencies we are interested in. First, we need to know how efficient the detector is at detecting β electrons created from ^{9}Li decay, and we need to know the efficiency for detecting the neutrons created by ^{9}Li decay. To estimate these efficiencies a Monte Carlo simulation package called GEANT4 was utilized in the

GLG4sim environment. GLG4sim is a Generic Liquid-scintillator Anti-Neutrino Detector Geant4 simulation. It is a common tool used to simulate neutrino related processes.

The simulation begins by creating a model of the actual detector for the program. It is a seven layer detector with the correct dimensions and physical composition. Four PMTs per layer were placed in their location for recording photons. Once the detector is created, particles of whatever type, energy, and momentum are flown in to the detector and the simulation models the physics of the interactions, recording such things as energy, time, and location of these interactions. Photons are created in the simulated liquid scintillator by these interactions which propagate through the volume of the detector and are eventually captured by the PMTs, just as in the real experiment. Data the detector records is then output, with some notable inclusions; the initial energy, momentum, time, location, and number are known. It is this fact that we take advantage of to determine an efficiency. Of course, this simulated efficiency is limited by the accuracy of the physics model in the simulation, and the result must be cross-checked with real data to ensure its reliability.

7.2.1 Simulated AmBe Source

In the process of calibrating the detector an AmBe radioactive source was placed just above the detector, showering the detector with neutrons and gammas. Monte Carlo simulation of this process is needed to compare with the real results, namely because with the simulated data the real number of neutrons and gammas sent into the detector is known. The neutron energy from the AmBe source is a spectrum from 4 to 8 MeV. For simulation purposes, 6 MeV was chosen as a fixed energy. 6543 neutrons were then isotropically released on top of the detector, and their interactions simulated by the program. Initially, loose cuts were applied to the data. The quenched energy deposit (recall equation 4.6) had to be greater than 0 MeV, and there had to be a recorded time since last neutron released between 1 ns and 10^7 ns. This reduced the neutrons down to 319. From there, the quenched energy deposit was required to be greater than 3 MeV, reducing the neutron count to 118. A time

Cut	Number
# Neutrons Primary	6543
$E_{depQ} > 0, \text{time} > 0$	319
$E_{depQ} > 3\text{MeV}$	118
$t_{min}(0.1\mu s) < t_{coinc} < t_{max}(200\mu s)$	83
$1 < N_{layer_{delayed}} < 4$	60
Efficiency	0.0092

Table 7.1: *Summary of cuts on Monte Carlo 6 MeV isotropic neutron data for neutrons incident from the top of the detector.*

cut was placed so that the time since the last neutron was greater than 0.1 μs but less than our 200 μs time window. The neutron count was then 83. Finally, the delayed signal was measured to see how many layers it was detected in. A proper delayed signal is considered one where 2 or 3 layers have a simultaneous signal present. 60 neutrons passed all of these cuts. Thus, the efficiency for this detector to measure neutrons coming from the top is

$$\epsilon_{neutrons_{top}} = \frac{60}{6543} = 0.0092. \tag{7.1}$$

See Table 7.1 for a summary.

The AmBe source also emits 4.43 MeV gammas with the neutron at a ratio of 1.5 neutrons per γ. MeV γ's interact with the matter in the detector by Compton scattering. In terms of energy, Compton scattering is described by

$$\frac{1}{E_{scattered}} = \frac{1}{E_{incident}} - \frac{(1-\cos\theta)}{m_e c^2}. \tag{7.2}$$

For maximum energy transfer, the scattered photon backscatters at $\theta = 180°$, leaving 4.17 MeV in the detector. This is the Compton peak, and all other energy deposits from γ's from the AmBe source will be less than this. To simulate the γ behavior, 4.17 MeV γ's were sent into the detector from the top at the same position as the neutrons. Similar cuts were applied to the γ's as the neutrons, with the exception of time window cuts since the γ is the prompt signal, not the delayed one. Also, we want the γ's that excited one layer of the box, not multiple layers. See Table 7.2 for a summary.

Cut	Number
# Γ's Primary	10000
$E_{depQ} > 0, \text{time} > 0$	1006
$E_{depQ} > 3\text{MeV}$	497
$N_{layer_{prompt}} = 1$	223
Efficiency	0.0223

Table 7.2: *Summary of cuts on Monte Carlo 4.17 MeV isotropic γ data for γ's incident from the top of the detector.*

Two Figures from the Monte Carlo data for γ's are shown. Figure 7.5 shows the layer-multiplicity for γ's. We are interested in a layer-multiplicity of one to simulate the result of β electrons in a real ^{9}Li event. Figure 7.6 shows the γ energy distribution. Recall all of the γ's started with an energy of 4.17 MeV.

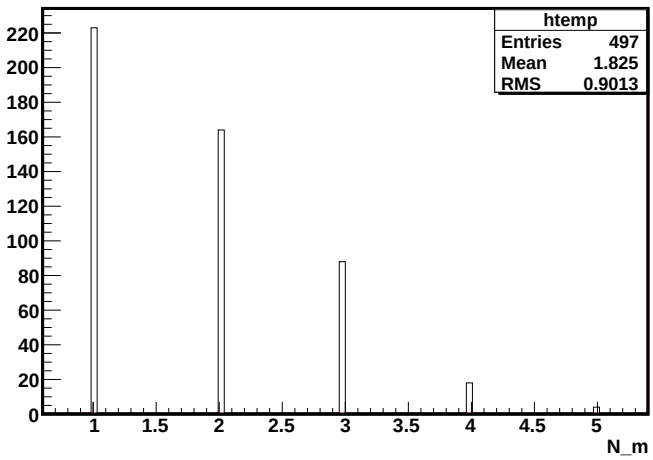

Figure 7.5: *From the Monte Carlo data for γ's, a plot of the layer-multiplicity. Recall these γ's are modeling γ's from an AmBe source. ^{9}Li has a β electron for a prompt, not a γ.*

Finally, the goal of simulating the AmBe source is to gain confidence in the Monte Carlo program's modeling of neutron and gamma interactions in the detector. To do this the neutron and γ Monte Carlo results for N_m (layer-multiplicity) were added together, and compared to the N_m data from the actual AmBe source.

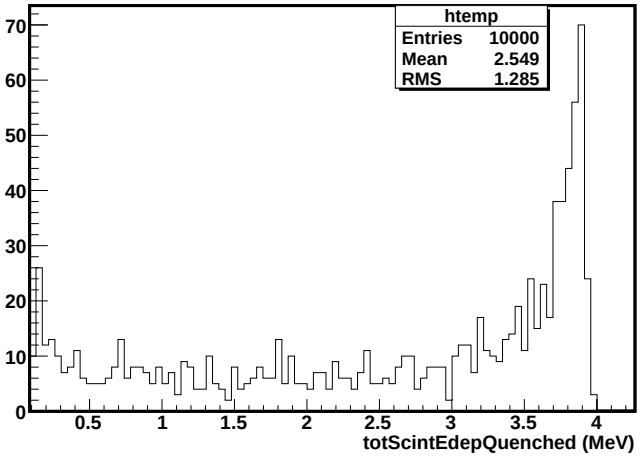

Figure 7.6: *From the Monte Carlo data for γ's, a plot of the γ quenched energy spectrum.*

Comparing these two plots requires some information and thought (See Figure 7.7). First, in the source data N_m = 1 is suppressed since there is a requirement that a delayed signal have layer-multiplicity of at least two. Second, note from Table 7.2 and Figure 7.5 that many γ's have N_m > 1 (Note that requiring them to be equal to 1 cut the number in half.). This means that γ's can trigger as a delayed signal in the detector. The AmBe source delayed signal histogram shown in Figure 7.7 contains, in addition to neutron captures, events that are actually γ's masquerading as the neutron capture signal. Third, in the source data, signals with a layer-multiplicity greater than three tend to be muons that traverse the detector and leave a large amount of energy. Placing a maximum energy requirement of 20 MeV on the delayed signal effectively limits the layer-multiplicity for the delayed signal to three or less. It is not fully known why this is the case. Looking then at N_m two and three, the basic shape observed in Monte Carlo and AmBe source data is the same. This means that the GLG4sim Monte Carlo simulation models the effects of γ's and neutrons in the real detector well.

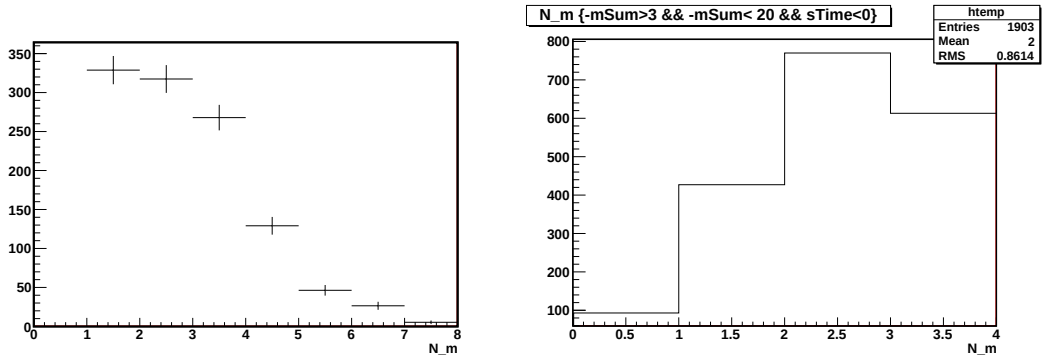

(a) Monte Carlo of AmBe

(b) AmBe source data

Figure 7.7: *Comparison of AmBe Monte Carlo and source data for layer-multiplicity. Note that in source data N_m = 1 is suppressed by a topological cut requirement. Source data for N_m 2 and 3 have the same basic shape and ratio as the Monte Carlo data. Notice the absence of N_m greater than 3 in the source data.*

7.2.2 Internal Neutron Monte Carlo Data

With the adequacy of GLG4sim to model neutron and γ behavior in the detector established, we use the Monte Carlo simulation to create neutrons inside the detector, just as neutrons will come from ^{9}Li decay. 30707 neutrons with energy 6 MeV were generated in the center of the detector, and given an isotropic momentum distribution. The same cuts were applied as to the earlier Monte Carlo. The results are summarized in Table 7.3.

Perhaps the most useful plot from this simulation is the capture time distribution for neutrons created inside the detector: Note that for times less than 200 μs this distribution

Cut	Number
# Neutrons Primary	30707
$E_{depQ} > 0, \text{time} > 0$	11749
$E_{depQ} > 3\text{MeV}$	6915
$t_{min}(0.1\mu s) < t_{coinc} < t_{max}(200\mu s)$	2843
$N_{layer_{prompt}}$	1302
Efficiency	0.0424

Table 7.3: *Summary of cuts on Monte Carlo 6 MeV isotropic neutron data for neutrons generated in the center of the detector.*

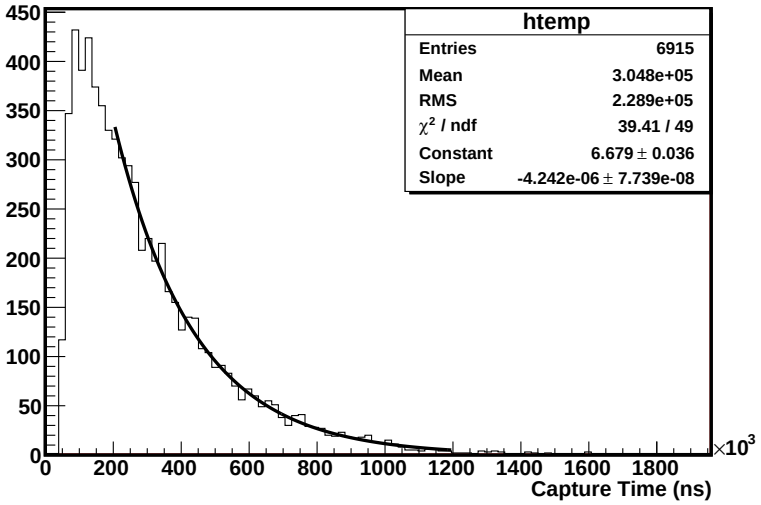

Figure 7.8: *From Monte Carlo, the distribution of the capture time for neutrons created inside the detector. The fit is for an exponential and yields a time constant $\tau = 235.7\ \mu s$.*

is essentially flat.

Another interesting plot is the neutron thermalization energy spectrum. Figure 7.9 shows that the energy is well below the 3 MeV threshold we have for signals.

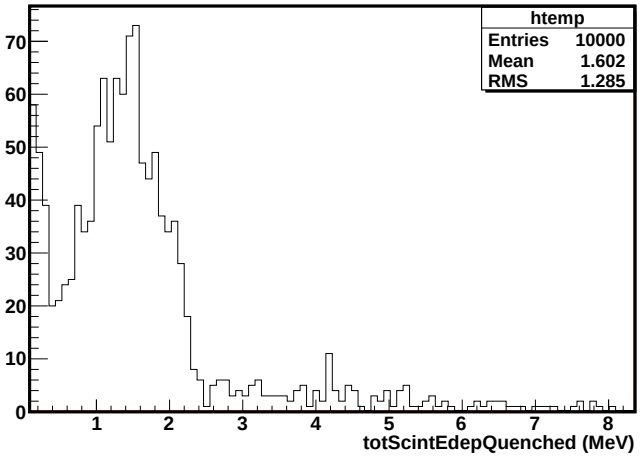

Figure 7.9: *From Monte Carlo, a look at the thermalization of the neutron. Note the peak is well below the 3 MeV threshold we apply on signals.*

7.2.3 Internal β Electron Monte Carlo

The last Monte Carlo simulation is on the β electron produced in ^{9}Li decay. β electrons are produced with a spectrum of energy values from 0 MeV up to about 11 MeV. To reproduce this distribution the β electron spectrum from ^{9}Li candidates at KamLAND was used[49]. Figure 7.10 displays this spectrum.

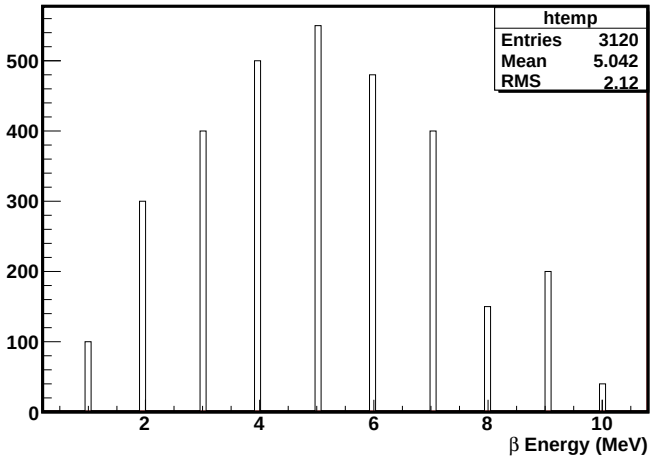

Figure 7.10: *From Monte Carlo, the β electron energy spectrum.*

The β electrons were introduced into the detector just as the internal neutrons. They were given an isotropic momentum distribution and started at the center of the detector. Figure 7.11 displays the layer-multiplicity results. As expected most β electrons deposit their energy in one layer only.

Table 7.4 summarizes the results of the β Monte Carlo. Notice that the main cut that limits the efficiency is the energy threshold requirement at 3 MeV.

7.3 Background

Now our eye is finally turned to the "real" data from which we will extract the ^{9}Li signal. To do so we need to know what is not a ^{9}Li signal, but still sneaks through all of our conditions. This signal is known as the background. We will measure it so that it can be subtracted

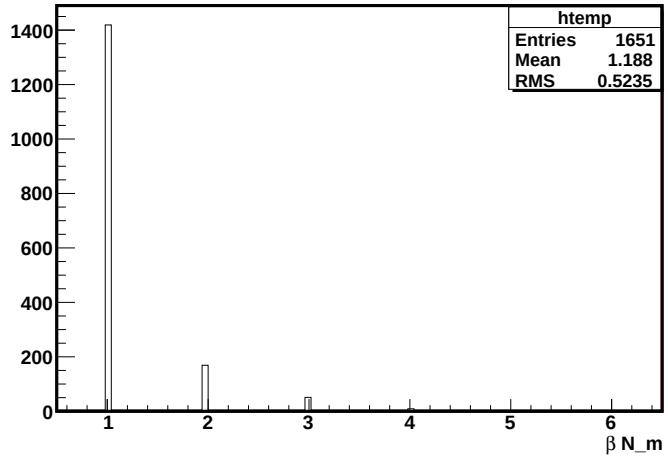

Figure 7.11: *From Monte Carlo, the β electron layer-multiplicity spectrum.*

Cut	Number
# β^- Primary	3120
$E_{depQ} > 0, \text{time} > 0$	3120
$E_{depQ} > 3\text{MeV}$	1651
$N_{layer_{prompt}}$	1419
Efficiency	0.4548

Table 7.4: *Summary of cuts on Monte Carlo isotropic β electron data for β electrons generated at the center of the detector. Notice the largest effect on the efficiency is the minimum energy requirement of 3 MeV.*

away from the detector signal. What remains will be ^{9}Li candidates. The data set we will use to establish the background signals represents 3.52 days (303,859 s) of data.

We will begin by looking at the raw detector signals. Figures 7.1 and 7.2 show the delayed signal in black. Figure 7.12 shows a similar view of the prompt signal with no cuts applied. Notice that the prompt signal background is exponential at low energies, and flat, or perhaps a "slow" exponential, at higher energies. Notice there are clearly two shapes in the background, an exponential at low energies, and a flat distribution that runs from low to higher energies. The exponential background comes from γ's entering the detector and triggering the detector, and the flat background comes from fast neutrons depositing

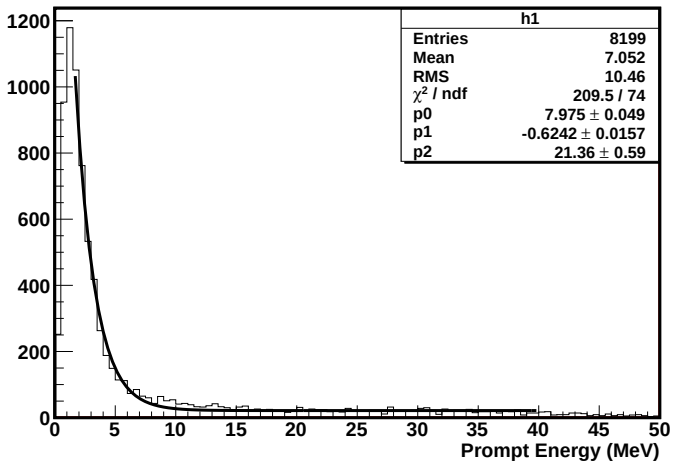

Figure 7.12: *A look at the background for the prompt signal. This plot is with only about 30 hours of data (the full background data set is about 84 hours), so there is little* ^{9}*Li signal. The fit is an exponential with a added constant parameter. There are no cuts on the data.*

energy as they traverse the detector. Also, note there is a slight hint of an extra signal in Figure 7.12 near the prompt signal range of 3 to 11 MeV.

A closer look is in order. Figure 7.13 shows the same raw prompt signal but with more data. Clearly there is something extra above the anticipated background of γ's and fast neutrons. To investigate this "extra" signal we subtracted the background fit functions in Figure 7.13 from that histogram. The result is plotted in Figure 7.14. There is clearly a signal remaining that our naive assumptions about the background did not anticipate.

One might assume at this point that this is not background, but is instead a clear ^{9}Li signal. This data represents only about 3.5 days worth of ^{9}Li production. From previous experimental results we anticipate at most something on the order of 10 ^{9}Li per day produced in the this detector (see Table 3.1). This rate, then, is much too high to be simply ^{9}Li since there are a few hundred events in question. Plus, as we shall see, there is no correspondingly large neutron capture signal. We thus conclude this signal is a part of the background we can not as of yet explain and not ^{9}Li.

To get a better handle on this "extra" background we applied a loose 50 MeV upper

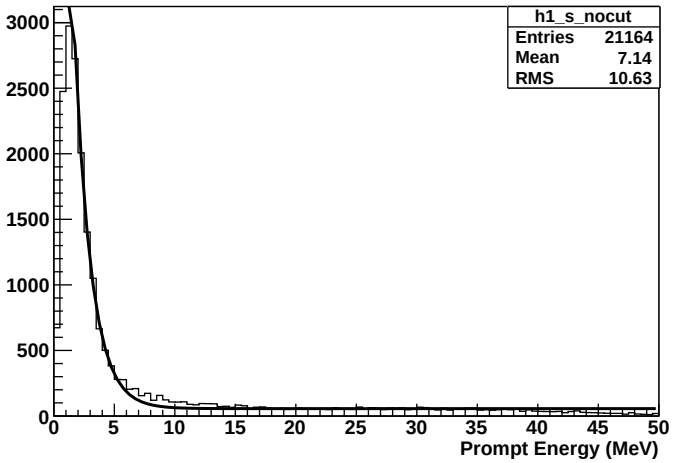

Figure 7.13: *Another look at the prompt signal with no cuts applied but with the full background data set. Notice the extra events in the signal range of 5 to 15 MeV.*

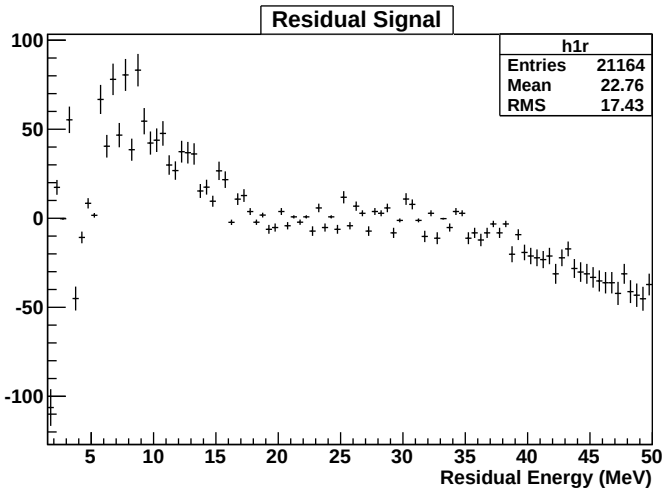

Figure 7.14: *The background fit functions (exponential for low energies plus a constant zero-degree polynomial) are subtracted from Figure 7.13. Notice there is clearly some signal remaining in the 3 to 11 MeV range.*

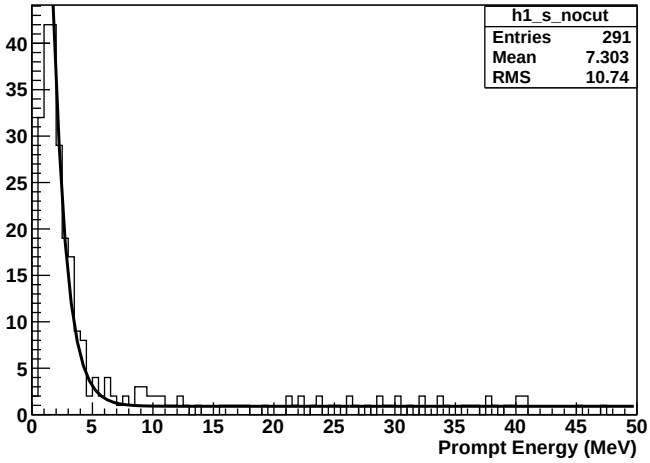

Figure 7.15: *A look at the background for the prompt signal with a loose delayed signal energy cut at 50 MeV. Notice that the extra events in the signal range of 3 to 11 MeV are drastically reduced.*

energy cut on the delayed signal (that is, we want delayed energies less than 50 MeV). The results are plotted in Figures 7.15 and 7.16. While the result is better than before, it is difficult to rule out this unanticipated background. Looking at the residual plot, there is still some potential for extra background to be present in the signal region. This means that estimating the signal contained in the prompt signal region from 3 to 11 MeV will be difficult until we get a better handle on what this "extra" background is.

We then turn to the delayed signal energy spectrum. First, we plot the delayed signal in the low energy region up to 50 MeV with no cuts applied (see Figure 7.17). The raw background is fit with a two-term linear function (A + Bx) in the range from 12 MeV to 45 MeV. The result is as noted in Figure 7.18. From there we apply all of the appropriate signal cuts: prompt energy $>$ 3 MeV but less than 11 MeV, delayed signal layer-multiplicity of 2 or 3, and time between prompt and delayed signal greater than 0 but less than 200 μs. Note that with these cuts we include the "extra" background in the prompt signal region in our background estimation, so we are safe to use the delayed signal as an effective estimate of the total background. We take the polynomial from Figure 7.17 and scale it to

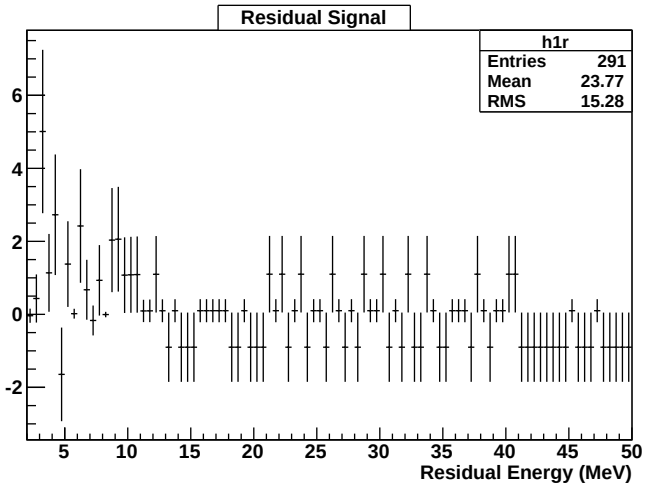

Figure 7.16: *The residual after the background functions are subtracted from the prompt signal with a 50 MeV upper delayed energy cut. Note that there is still enough potential "extra" background left in the signal region of 3 to 11 MeV to question whether all of the background has been properly accounted for.*

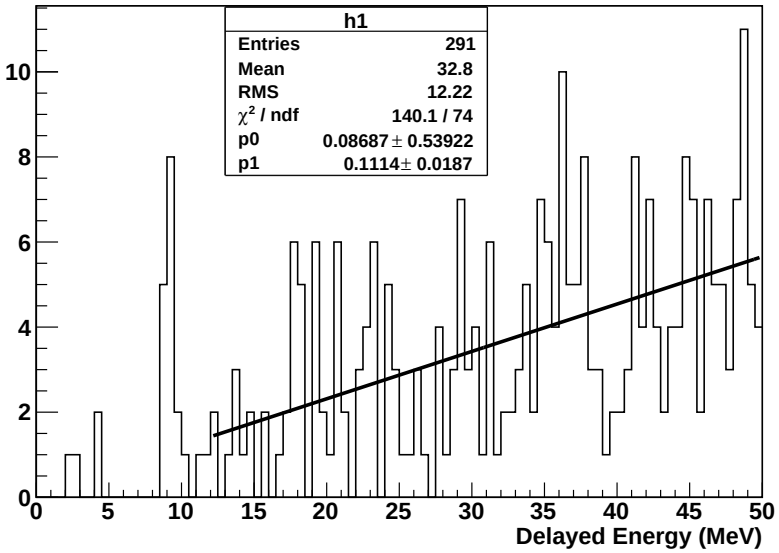

Figure 7.17: *A look at the background for the delayed signal energy with no cuts. The fit is for a linear function.*

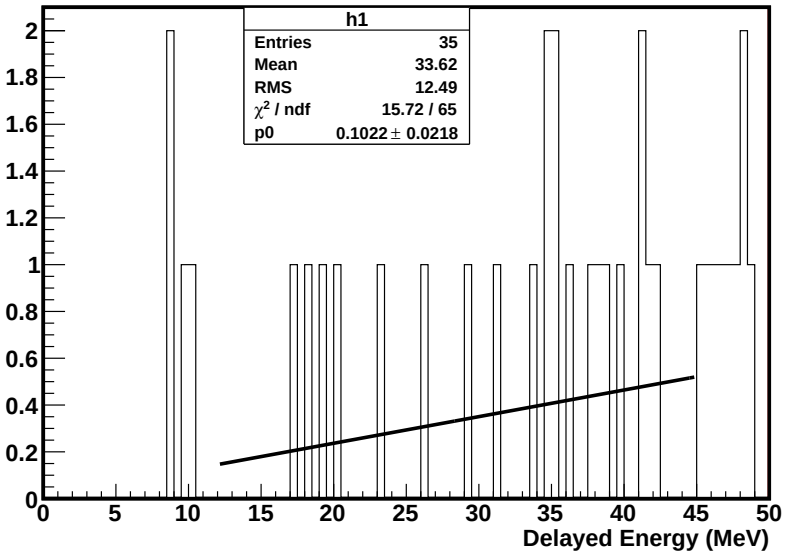

Figure 7.18: *A look at the background for the delayed signal energy with signal cuts applied. A fit with the linear function determined in Figure 7.17 is scaled to fit here.*

this histogram with all of the cuts applied (Figure 7.18). The fitted constant here is a scale factor multiplied with the linear polynomial in Figure 7.17 assuming only the mean values:

$$\mathrm{BG_{delayed}} = \mathrm{p0} * (0.08687 + 0.1114 * \mathrm{E_{delayed}}) \text{ per } 0.5 \text{ MeV bin}, \tag{7.3}$$

where p0 is found to be 0.1022 ± 0.0218.

Chapter 8

Data Results

Now we finally come to preliminary results for this experiment. It is important to realize that this experiment will collect data for several months. We will now report results for same data used to perform the background measurements in chapter 7, or about 3.5 days worth of data collection.

8.1 A Look at the Signal Region

We begin by looking at the signal region of the delayed signal energy spectrum with full cuts applied. We then count the number of events observed. The full cuts are prompt signal energy $>$ 3 MeV but less than 11 MeV, layer-multiplicity for the delayed signal of 2 or 3, a time difference between prompt and delayed signal $>$ 0 but less than 200 μs, and then a delayed signal energy range of 6 to 11.5 MeV. See Figure 8.1. We observe 4 events.

If we apply the same cuts to the prompt signal energy and the time difference between prompt and delayed signal, we see the same count, 4 observed events (see Figure 8.2).

8.2 Reporting a Rate

The ultimate goal of this experiment is to report a rate for ^{9}Li production. The rate will be reported as a number per day per ton of liquid scintillator. At this point, something should be made clear. What the process described in this thesis has determined is a number

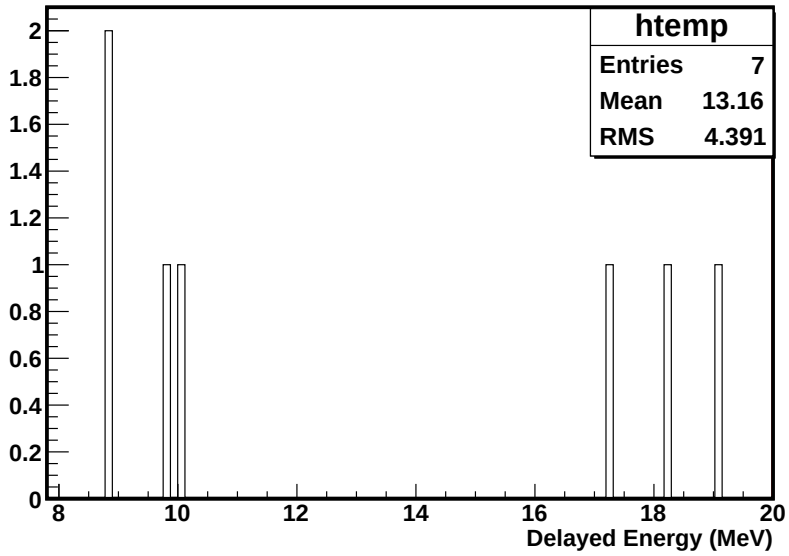

Figure 8.1: *A look at the signal region for the delayed signal energy with all cuts applied. There are 4 observed events between 6 and 11.5 MeV.*

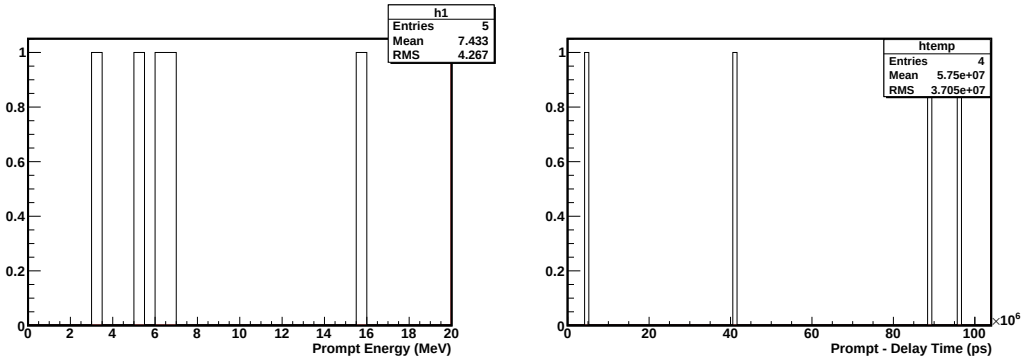

(a) Signal region for prompt signal energy

(b) Prompt and delayed signal time difference in signal region

Figure 8.2: *Confirmation that the applied cuts are consistent. Here, the prompt signal energy and time difference both yield 4 observed events, just as the delayed signal energy. Recall the prompt signal range is from 3 to 11 MeV.*

of ^{9}Li-like candidates that have prompt signal in one layer within the appropriate energy region, and a delayed signal with the appropriate layer-multiplicity and energy. What this procedure does not do is tie this signal to a passing previous muon, which is required for saying that cosmic ray muons produce these ^{9}Li-like candidates. Future data-taking will do so.

For now, let us proceed with the estimation of the production rate of these ^{9}Li-like candidates. The ^{9}Li-like production rate formula is

$$^9\text{Li} - \text{like Rate} = \frac{\text{S}}{\epsilon_{\text{Li}}\ \text{t}_{\text{live}}\ m_{\text{detector}}}. \tag{8.1}$$

S is the ^{9}Li-like signal count, ϵ_{Li} is the efficiency of the detector, t_{live} is the detector live time, and m_{detector} is the mass of the liquid scintillator present in the detector. We will examine each factor in detail.

8.2.1 Efficiency, Live Time, and Volume Estimation

We begin by looking at the systematic error factors in the rate estimation. A summary is contained in Table 8.1. First, recall the detector efficiencies that we estimated from the Monte Carlo simulation of the detector. We need to divide by this efficiency to get the "real" signal count if our detector were perfect. This efficiency is the product of the internal neutron efficiency and the internal β efficiency.

$$\epsilon_{\text{Li}} = \epsilon_{\text{neutron}_{\text{int}}} * \epsilon_\beta = 0.0424\ *\ 0.4548 = 0.01928 \tag{8.2}$$

There is also an error on this efficiency estimation. Primarily, our efficiency relies upon our energy calibration. This uncertainty comes from the way we performed the energy calibration. We used the approximation that vertical muons deposit 2 MeV per cm traversed. The actual value depends upon the liquid scintillator used. Bicron, the scintillator manufacturer, provided no detailed information on this value. Using other approximations from the Particle Data Group website, one can estimate that similar liquid scintillator might have a muon energy deposit per length of 1.83 MeV per cm[50]. Call this error around 20%. Another

Factor	Number	Error
Efficiency	0.019	0.0039
Live Time	2.937 days	0.018
Detector Mass	0.62 tons	0.031

Table 8.1: *A listing of the systematic errors in this experiment.*

source of energy uncertainty is that each layer is not fully filled with scintillator up to the full 10 cm. Perhaps the level is uncertain to about 5%. Thus, to be conservative, we arrive at an error of $\sqrt{(0.2)^2 + (0.05)^2} \approx 0.2$, or 20%. Therefore, the efficiency with uncertainty is

$$\epsilon_{\mathrm{Li}} = 0.01928 \pm 0.0039. \tag{8.3}$$

The rate also has a dependence upon the time the data was taken over. In this case, the reported time is 303,859 s (3.5169 days). There is an uncertainty in the live time of the detector however. While the computer is writing data, the detector is effectively dead. Any signals that would trigger the detector during this time will be missed. To estimate this a signal counter was used to record the number of total events the DAQ system tried to trigger, and compared it with the number the computer actually recorded. The result was a (16.5 ± 0.5)% dead time. This is equivalent to a live time of (83.5 ± 0.5)%. For the time this data represents, that is 2.937 ± 0.018 days.

Finally, the rate depends upon the amount of liquid scintillator in the detector. Recall that each layer of the detector has interior dimensions of 1.25 m x 0.75 m x 0.10 m. This yields 0.09375 m^3 per layer. There are seven layers, so the total enclosed volume is 0.6563 m^3. The difficulty is that this total volume is not completely filled and we did not measure the amount of scintillator loaded into the detector. We must then estimate the error on the volume of the detector. We estimate that no layer is filled to less than 95% of its volume, so I will use 5% as an estimate on the volume error. To complete the scintillator tonnage measurement, we note that the density of Bicron 517L is 860 $\frac{\mathrm{kg}}{\mathrm{m}^3}$ [47]. This yields 0.62 ± 0.031 tons.

8.2.2 Background Estimation

Next, we use the background information that we determined in chapter 7 to estimate the background in the delayed signal region. Equation 7.3 tells us the number of background events per bin for the delayed signal. The signal region is from 6 to 11.5 MeV. Integrating this function over that interval and accounting for the bin size yields a value of 1.19 ± 0.25. Then, the estimator for the background count becomes

$$\hat{\mathrm{B}} = 1.19 \pm 0.25. \tag{8.4}$$

8.2.3 A Rate Upper Limit

With the errors in this experiment estimated, we are now prepared to report a 90% significance level upper limit on the ^{9}Li-like production rate. As stated earlier, the rate equation is

$$^9\mathrm{Li-like\ Rate} = \mathrm{R} = \frac{\hat{\mathrm{S}}}{\epsilon_{\mathrm{Li}}\ \mathrm{t}_{\mathrm{live}}\ m_{\mathrm{detector}}}. \tag{8.5}$$

In this equation, $\hat{S}$ is the estimation of the signal. That is the estimation of the number of ^{9}Li-like events. We want to place an upper limit on this number.

There is perhaps more than one way to do this, but we will proceed as follows. We have two types of information to determine this upper limit. We have the estimations in the errors, and we have the number of ^{9}Li-like events that we counted, 4. We assume that the four errors we estimated, background, efficiency uncertainty, live time uncertainty, and liquid scintillator mass uncertainty, are Gaussian in distribution. We also know that the number of observed ^{9}Li-like candidates are distributed Poisson. From Equation 8.5, we also know that the signal S is

$$S = \epsilon_{\mathrm{Li}}\ t_{\mathrm{live}}\ m_{\mathrm{detector}}\ R. \tag{8.6}$$

Another piece of information is that the number of observed events, N, is described by

$$N = S + \hat{B} \tag{8.7}$$

A 90% significance level upper limit on the rate would be a number S_{UL} that, when added with the background estimation, is the mean of a Poisson distribution representing the observed number of events N which only 10 % of the time has a number less than or equal to 4. Said another way, 90% of the time this distribution would have a number greater than 4.

To find this upper limit we generate this Poisson distribution with a random number generator. The mean μ of the observed number of events N is

$$\mu_N = \hat{\epsilon}\, \hat{t_{live}}\, \hat{m}\, R_{\mathrm{UL}} + \hat{B}. \tag{8.8}$$

Each error in Equation 8.8 is assumed to be distributed Gaussian, so a Gaussian number from the appropriate Gaussian distribution (see Table 8.1 and Equation 8.4) is generated. These numbers are then used to calculate the mean according to Equation 8.8 given a test value for the rate upper limit. This mean is then used to generate a random number from a Poisson distribution, and that value is binned in a histogram. The process is repeated for a total of 1,000,000 times. The resulting histogram is then integrated to see how many times the result was 4 or less. The 90% significance level upper limit on the rate is the test value that returns a result of 10% of the events in the resulting histogram being 4 or less.

Following this procedure with a test value of 213 ^{9}Li-like events per day per ton yields the histogram in Figure 8.3. Thus, we report a 90% significance level upper limit on the ^{9}Li-like rate of 213 per day per ton.

As a cross-check, we looked at a "lower limit" of 0 (by doing this we "turn off" the ^{9}Li-like rate and just look at the background contribution to see how likely the background alone would produce an observed count of N = 4.) by following the above procedure but fixing the test value at 0. The resulting histogram is shown in Figure 8.4. Only 4% of the time will background-only fluctuate up to an observed count N of 4 or greater. We are thus relatively confident that the detector observes ^{9}Li-like signals above background.

We conclude with a brief discussion about the sensitivity of this experiment to measure ^{9}Li-like signals above background. The background for this data-taking period was found to

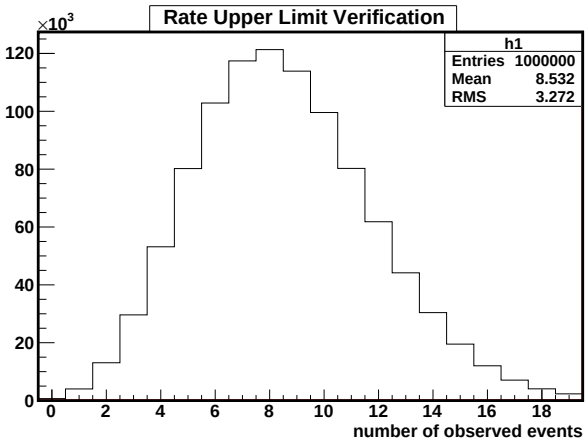

Figure 8.3: *Shown is the result of 1,000,000 simulated "experiments". A random mean using Equation 8.8 was determined from a fixed test value R_{UL} of 213.0 ^{9}Li-like events per day per ton for the rate upper limit and random numbers for the given errors assuming a Gaussian distribution for each. This mean was used to generate a number from a Poisson distribution, and the result was binned. In this simulation, 100,546 "experiments" had $N = 4$ or less, or approximately 10%.*

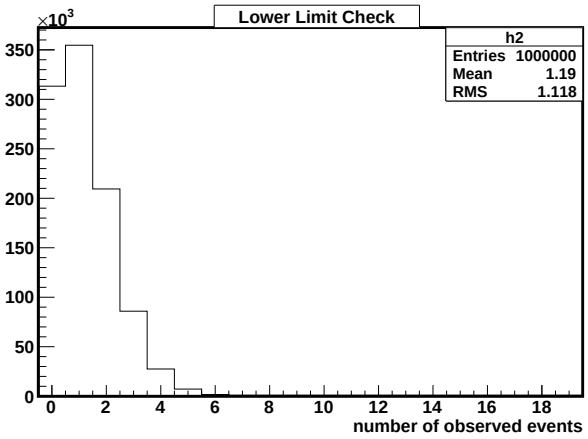

Figure 8.4: *Shown is the result of 1,000,000 simulated "experiments". A random mean using Equation 8.8 was determined from a fixed test value R_{UL} of 0 and random numbers for the given errors assuming a Gaussian distribution for each. This mean was used to generate a number from a Poisson distribution, and the result was binned. In this simulation, 36,758 "experiments" had an N greater than or equal to 4,or approximately 4%. This means that our observed count of $N = 4$ is consistent with observing some non-background ^{9}Li-like signal counts 96% of the time.*

be 1.19 ± 0.25. If 16 times more data were taken, then the background would be expected to be:

$$\hat{B} = (16 \times 1.19) \pm (\sqrt{16 \times 1.19}_{stat} \pm \sqrt{16 \times 0.25^2}_{sys}) = 19.04 \pm (\sqrt{19}_{stat} \pm 1_{sys}). \quad (8.9)$$

The uncertainty in the background count would then be about $\sqrt{20}$. The experiment would then be sensitive at the 2 σ level to a signal count of $2 \times \sqrt{20} \approx 9$ above background only. Accounting for the detector efficiency and live time, this sensitivity becomes a ^{9}Li-like rate for this detector of

$$R_{\text{Sensitive}} \approx \frac{9}{0.019 \times 47 \text{ days}} \approx 10 \text{ per day}. \quad (8.10)$$

Bibliography

[1] W. Pauli, Physics Today **31**, 27 (1978), (translation into English).

[2] J. Chadwick, Nature **129**, 312 (1932).

[3] J. Chadwick, Proc. Roy. Soc. **A136**, 692 (1932).

[4] E. Fermi, Z. Phys. **88**, 161 (1934).

[5] E. Fermi, Nuovo Cim. **11**, 1 (1934).

[6] B. Pontecorvo, Chaulk River Laboratory Report PD-205, 1946, (unpublished).

[7] F. Reines and C. L. Cowan, Phys. Rev. **92**, 830 (1953).

[8] T. D. Lee and C.-N. Yang, Phys. Rev. **104**, 254 (1956).

[9] C. S. Wu et al., Phys. Rev. **105**, 1413 (1957).

[10] M. Goldhaber, L. Grodzins, and A. W. Sunyar, Phys. Rev. **109**, 1015 (1958).

[11] G. Danby et al., Phys. Rev. Lett. **9**, 36 (1962).

[12] S. L. Glashow, Nucl. Phys. **22**, 579 (1961).

[13] A. Salam and J. C. Ward, Phys. Lett. **13**, 168 (1964).

[14] S. Weinberg, Phys. Rev. Lett. **19**, 1264 (1967).

[15] R. Davis, D. S. Harmer, and K. C. Hoffman, Phys. Rev. Lett. **20**, 1205 (1968).

[16] S. N. Ahmed et al., Phys. Rev. Lett. **92**, 181301 (2004).

[17] H. Faissner et al., Phys. Rev. Lett. **41**, 213 (1978).

[18] H. Faissner et al., Phys. Rev. Lett. **41**, 1083 (1978).

[19] J. Blietschau et al., Nucl. Phys. **B114**, 189 (1976).

[20] M. L. Perl et al., Phys. Rev. Lett. **35**, 1489 (1975).

[21] M. L. Perl et al., Phys. Lett. **B63**, 466 (1976).

[22] M. L. Perl et al., Phys. Lett. **B70**, 487 (1977).

[23] K. Kodama et al., Phys. Lett. **B504**, 218 (2001).

[24] G. S. Abrams et al., Phys. Rev. Lett. **63**, 2173 (1989).

[25] R. M. Bionta et al., Phys. Rev. Lett. **58**, 1494 (1987).

[26] K. Hirata et al., Phys. Rev. Lett. **58**, 1490 (1987).

[27] K. Eguchi et al., Phys. Rev. Lett. **90**, 021802 (2003).

[28] S. Abe et al., Phys. Rev. Lett. **100**, 221803 (2008).

[29] C. Amsler, Phys. Lett. **B667**, 1 (2008).

[30] B. Pontecorvo, JETP **33**, 549 (1957).

[31] B. Pontecorvo, JETP **34**, 247 (1958).

[32] B. Pontecorvo, Zh. Eksp. Teor. Fiz. **53**, 1717 (1967).

[33] Z. Maki, M. Nakagawa, and S. Sakata, Prog. Theor. Phys. **28**, 870 (1962).

[34] B. Kayser, Neutrino physics, arXiv:hep-ph/0506165v1, 2005.

[35] R. D. Jr, D. Harmer, and K. Hoffman, Phys. Rev. Lett. **20**, 1205.

[36] D. J. Griffiths, *Introduction to Elementary Particles*, New York: Wiley, 1987, Much of the section of chapter 2 on CP violation is inspired by Griffiths' book, sections 4.8 and 4.9.

[37] M. Gell-Mann and A. Pais, Phys. Rev. **97**, 1387 (1955).

[38] K. Lande et al., Phys. Rev. **103**, 1901 (1956).

[39] J. H. Christenson et al., Phys. Rev. Lett. **13**, 138 (1964).

[40] G. Horton-Smith, Toward new discoveries at low-energy neutrino experiments, DOE Outstanding Junior Investigator Proposal, 2004, (Much of the content of this section has been adapted from this reference, which is the proposal that led to this experiment.).

[41] D. A. Dwyer, *Measurement of Neutrino Oscillation with KamLAND*, PhD thesis, Stanford University, 2007.

[42] F. Ardellier et al., Letter of intent for double chooz, arXiv:hep-ex/0405032, 2004.

[43] T. Hagner et al., Astropart. Phys. **14**, 33 (2000).

[44] G. Horton-Smith, J. Atwell, R. McKeown, and P.Vogel, Quashing backgrounds, Presentation at the Workshop on Future Low Energy Neutrino Experiments, Technical University Munich, Munich, October 9-11, 2003.

[45] http://nndc.bnl.gov/nudat2/wcbyz.jsp?z=3.

[46] http://nndc.bnl.gov/.

[47] http://www.detectors.saint-gobain.com, "BC-517S, BC-517H, BC-517L, BC-517P Mineral Oil Based Liquid Scintillators", Browsed May 18,2009.

[48] A. de Capoa, Calibration of the fd telescope channels using light pulses, GAPNote, GAP2002-005, 2002.

[49] J. Detwiler, *Precision Measurement of Neutrino Oscillation Parameters with KamLAND*, PhD thesis, University of California, Berkeley, 2005.

[50] C. Amsler, Phys. Lett. **B667**, 1 (2008), See this website: http://pdg.lbl.gov/2008/AtomicNuclearProperties/index.html. Look under "simple organic compounds" for materials similar to dodecane, the primary component of Bicron 517L liquid scintillator. Browsed May 18, 2009.

Appendix A

A Look at the Detector

This appendix shows pictures of the detector itself and has a brief description of the physical make-up of the detector. Let us begin by taking a look at the full detector (see Figure A.1). What is seen here are the eight individual layers of the detector, with four layers on the side

Figure A.1: *A look at the full detector with most of the boron-loaded plastic shielding removed.*

shown, and the other four perpendicular to this side. Note that each end of each layer has ports for two photomultiplier tubes. Several things should be noted at this point. First, the purple plastic sheets on the top and right side are the boron-loaded plastic shielding to reduce external thermal neutrons. The detector is completely covered by this shielding when in operation. Second, the layers of the detector are supported by a Unistrut frame (see Figure A.2 for a close-up example), with each end of each layer having a Unistrut beam under it. Each layer has a fill/drain valve to enable liquid scintillator to be loaded in or

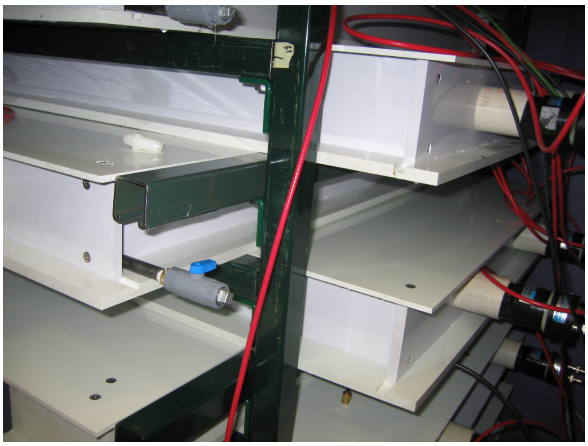

Figure A.2: *A close-up look at the detector. Notice the green Unistrut frame to support the weight of the layers. Also note the fill/drain valve (gray with blue knob) used to pump liquid scintillator in and out of the layer.*

out of each layer. When filled, a plug is inserted to prevent accidental spills if the valve is unintentionally opened.

We now move inside a layer of the detector. Remember that each layer is constructed from PVC (poly-vinyl chloride). The sides, top and bottom have grooves machined out to fit the pieces together. The joints of each layer are then sealed with RTV approved for use with pseudocumene. The RTV sealant combined with a tight machined fit made for little leakage of the liquid scintillator. Figure A.3 gives a view inside of a layer filled with liquid scintillator. The left side, (a), of Figure A.3 shows a properly filled layer. Notice the nice

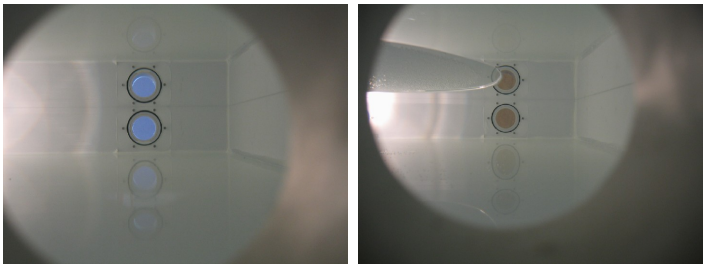

(a) A liquid scintillator-filled layer

(b) A layer that is over-filled

Figure A.3: *An internal look at a layer of the detector filled with liquid scintillator.*

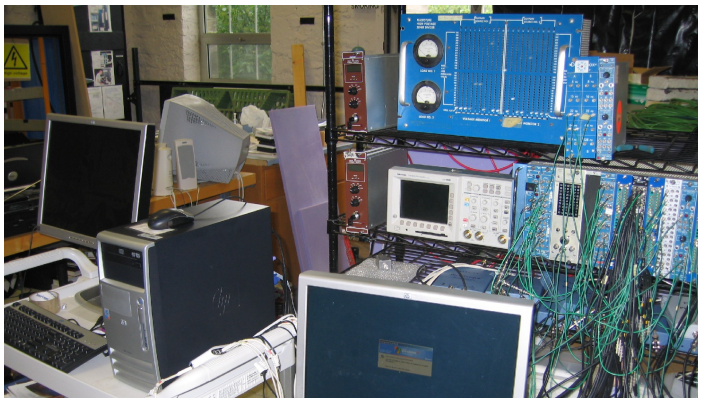

Figure A.4: *A look at the DAQ system. The computers are in the foreground, and the electronics are behind on the rack.*

Figure A.5: *A close-up look at the power supplies (two brown boxes on left side) and the power voltage divider (center).*

mirror-image on the top caused by the total internal reflection of the liquid scintillator-air interface at the top of each layer. If the layer is over-filled, the liquid scintillator touches the top of the box and the total internal reflection effect is ruined (see the right side, (b), of Figure A.3).

We now take a look at the DAQ system. Figure A.4 shows a full view of the DAQ system. Figure A.5 shows a close-up of the power supply and power voltage divider. Figure A.6 shows a close-up of the rest of the electronics in the DAQ system. Finally, Figure A.7

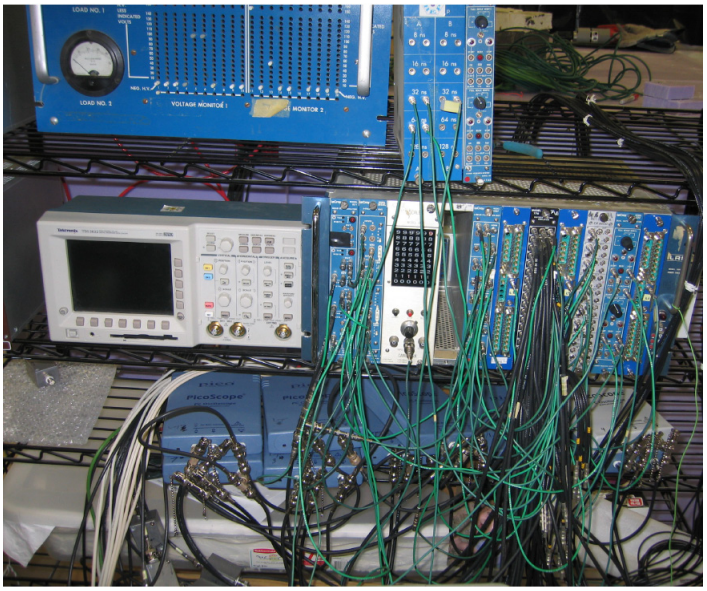

Figure A.6: *A close-up look at the rest of the electronics in DAQ system. Top left is the voltage divider. Top center is a delay box. In the NIM crate from left to right: a quad discriminator, a four-fold logic unit , a counter, a linear fan-in/fan-out, another linear fan-in/fan-out, a 16-channel amplifier, another linear fan-in/fan-out, a constant fraction discriminator, a dual gate generator, and another linear fan-in/fan-out. Just below the NIM crate are the PC oscilloscopes.*

Figure A.7: *A close-up look at a PicoScope 3205 PC oscilloscope.*

features a close-up view of a PicoScope 3205 PC oscilloscope.